Materials Reports: Energy 3 (2023) 100198

Contents lists available at ScienceDirect

Materials Reports: Energy

journal homepage: www.keaipublishing.com/en/journals/materials-reports-energy

Review

Exsolved materials for CO_2 reduction in high-temperature electrolysis cells

Min Xu [a,b], Ran Cao [a,c], Han Qin [a,d], Nuoxi Zhang [e], Wenle Yan [a,c], Liming Liu [a], John T.S. Irvine [e], Di Chen [a,*]

[a] The Future Laboratory, Tsinghua University, Beijing, 100084, China
[b] Academy of Arts & Design, Tsinghua University, Beijing, 100084, China
[c] Weiyang College, Tsinghua University, Beijing, 100084, China
[d] School of Materials Science and Engineering, Tsinghua University, Beijing, 100084, China
[e] School of Chemistry, University of St Andrews, St Andrews, Fife, KY16 9ST, UK

ARTICLE INFO

Keywords:
CO_2 reduction
Exsolution
Solid oxide electrolysis cells
Catalysts

ABSTRACT

Electrochemical reduction of CO_2 into valuable fuels and chemicals has become a contemporary research area, where the heterogeneous catalyst plays a critical role. Metal nanoparticles supported on oxides performing as active sites of electrochemical reactions have been the focus of intensive investigation. Here, we review the CO_2 reduction with active materials prepared by exsolution. The fundamental of exsolution was summarized in terms of mechanism and models, materials, and driven forces. The advances in the exsolved materials used in high-temperature CO_2 electrolysis were catalogued into tailored interfaces, synergistic effects on alloy particles, phase transition, reversibility and electrochemical switching.

1. Introduction

The unprecedented increased energy consumption creates the civilization of our modern world but unavoidably coupled with the emission of contamination compounds to the environment, including nitrous oxides, sulfur oxides, volatile organic compounds and CO_2. The excessively released CO_2 into the atmosphere absorbs infrared heat and has recently been a concerned cause to global warming as a result of burning fossil resources.[1,2] Converting CO_2 into oxygen and other high-value fuels is essential for not only achieving low-carbon energy but also powering the exploration of space.[3,4]

The reduction of CO_2 to target products is restricted by the strong C═O bonds (805 kJ mol^{-1}) in the linear molecules. Powered by intermittent energy, electrolyzers are promising to achieve the aforementioned goals. Solid oxide electrolysis cells (SOECs) possess advanced features, including high operating temperatures and the ability to integrate with downstream chemical syntheses.[5–7] In CO_2 SOECs, gases directly diffuse to the solid electrodes and are electro-reduced/oxidized to products. SOECs have been explored for years to develop high efficiency and stability, while this conversion technique is still far from a market requirement.

Among various challenges, the development of efficient materials is crucial for further improving efficiency and stability. Metal electrodes were first applied on SOECs, however, they normally exhibit lower exchange current densities.[8,9] Ni metal has relatively lower prices and possesses high catalytic activity, thus, attracting more attention. To endow high ionic conductivity for the electrode, ionic oxides were added to the metal system, such as Ni/yttria stabilized zirconia (YSZ) cermet which is the most common cathode material for CO_2 SOEC. The coupling between Ni (electron conductor) and YSZ (ion conductor) provides more triple-phase boundary (TPB) which acts as the active site for the reaction.[10–12] However, the large amount of utilized Ni metal causes degradations including volume change (during redox), agglomeration and coking. Reducing gases are normally necessary to protect the cermet electrode during operation unless a high electrolysis voltage is applied.[13,14]

Mixed ion and electron conductors demonstrate the potential to tackle the aforementioned issues, due to their flexibility in redox

* Corresponding author.
E-mail address: dichen@tsinghua.edu.cn (D. Chen).

Production and Hosting by Elsevier on behalf of KeAi

https://doi.org/10.1016/j.matre.2023.100198
Received 22 February 2023; Received in revised form 6 April 2023; Accepted 9 April 2023
Available online 27 April 2023

atmosphere and the entire active surface.[15,16] However, their limitation has been inferior catalytic reactivity compared to Ni/YSZ. Recently, the exsolution of nanoparticles on electrodes has exhibited promising performance in CO_2 SOECs.[17] The exsolved nanoparticles form an embedded structure in the support, a trait that makes it useful as an active support in solid oxide electrochemical cells. The supported nanoparticles together with the active dopants seem to be an efficient method for facilitating CO_2 reduction.[18–20] Metal nanoparticles play a crucial role in improving the activity and the stability of CO_2 reduction. The performance of SOECs is determined by types of metal nanoparticles, the interface of metal-oxides and properties of support oxides.[21,22]

In this review, we summarize the current advances in CO_2 SOECs with exsolved materials. We briefly introduce the fundamentals of exsolution and CO_2 electrochemical reduction, followed by the development of electrochemical CO_2 reduction based on nanoparticle-supported materials. In addition, we summarize the mechanism of improvement for utilizing those electrodes by reviewing various literature on the exact exsolution objects. The challenges and perspectives will be concluded on the advancements that are required to make this system feasible and efficient.

2. Exsolution fundamentals

In contrast to traditional deposition techniques, exsolution is an 'inside-out' technique that produces precipitation in a solid-phase solution. Exsolution involves two phases from a solid solution that becomes unstable on redox or cooling processes. Exsolution offers an alternative way to anchor the nanoparticles on parental materials, thus providing excellent stability. Generally, catalytic nanoparticles emerge by phase separation in the exsolution process. The process of exsolution can be described as metal-oxide chemical bonds breaking in the solid solution, making it easy to reveal its lattice mechanism. Here, theoretical routes based on segregation energy, thermodynamic model and driven forces will be discussed.

2.1. Oxygen vacancy and segregation energy

A mechanism that explains the driving force of exsolution is the cations diffusion accompanied by the lattice oxygen loss. Deliberate removal of oxygen to the opposite side causes irritability for the lattice which expels the cation out as a response, such as in A-site deficient perovskite[23]:

$$A_{1-\alpha}BO_3 \overset{\text{Reduction}}{\rightarrow} A_{1-\alpha}B_{1-x}O_{3-\delta} + xB + \frac{\delta}{2}O_2 \tag{1}$$

where the B-site cation exsolved out from the lattice to re-establish stoichiometry when the oxygen vacancies reach a sufficiently high concentration. The loss of oxygen engenders the developed model of the redox process. The extent of reduction is generally extrinsically determined by the temperature and oxygen partial pressure effects that can be denoted by the chemical potential (μ_0)[24,25]:

$$\mu_0(T,p) = \frac{1}{2}\left[\mu_0(T) + kTln(p)\right] \tag{2}$$

In exsolution, metal segregation is correlated with the formation of oxygen vacancy. Segregation energy based on the density functional theory (DFT) method was developed on the exsolution of both noble metals and transition metals.[26,27] The segregation energy is normally defined as the energy difference between the slab surface with metal atoms and the bulk with metal cation in the lattice:

$$E_{seg} = E_{surface} - E_{bulk} \tag{3}$$

From this model, chemical defect influence can be concluded as the coulombic attraction between the vacancies and deficiencies. With the combination of the chemical potential of oxygen and surface energy, this model is associated with the exsolution trend of metal and the significant effect of oxygen vacancy. The segregation energies of Pd, Rh and Pt doped $LaFeO_3$ were calculated based on the ab initio thermodynamics calculation of Gibbs free energy and oxygen chemical potential. The calculated E_{seg} shows that the surface segregation of Pd is favorable over a wide range of oxygen partial pressure.[26] In comparsion, the Pt is stable only below 1.0×10^{-4} atm at 1000 K. The thermodynamic potential was also employed to study the phase equilibria in Pt doped $CaTiO_3$ in regards of the influence of temperature, pressure and oxygen chemical potential.[24] The study shows that the self-regenerative effect of Pt is a consequence of thermodynamic phase stability under redox conditions. The value of segregation energy is performed to describe the possibility of exsolution for a certain system. A more negative segregation energy value generally indicates ready exsolution, while a smaller value indicates a hard exsolved case.[28,29] The smaller segregation energy of certain orientation or termination can be used to understand the surface preferential of emerged particles.[27] This model is also applicable for the exsolution of double perovskites (DP) and links the transition metal exsolution with vacancy formation energy.[30]

Though the exsolution is normally the segregation of cations on B-site in perovskite, the analogy on A-site segregation study is worthy of reference here. It has been shown that the surface segregation of A-site cation is proportional to its radius size.[31] Gradient energy and defect interactions were considered in a surface-mediated model using a phase-field approach.[32] A first-order phase transition may occur depending on the strength of dopant interactions and the affinity of dopants cations and oxygen vacancies for the free surface. However, a holistic, quantitative thermodynamic framework has not yet been established.

2.2. Phase transition and thermodynamic model

The exsolution was taken as a chemically driven heterogeneous phase transformation, including four physical processes, namely diffusion, reduction, nucleation and growth, as shown in Fig. 1a. Regarding the phase transformation, we are always concerned with the changes towards equilibrium, therefore, thermodynamics is a potent tool. Exsolution was triggered when the solid solution was saturated leading to an unstable initial state. Thus, phase separation formed to further stabilize the solid solution system. Thermodynamics provides an answer to how to measure the exsolution stability. The classical isothermal nucleation theory describes nucleation as a process attributed to the Gibbs free energy of the nucleus at the critical particle size (r^*) and the nucleation rate ($\dot{N}$), as shown in Fig. 1b, which can be expressed as:[33]

$$\dot{N} = \frac{C}{\tau}\exp\left(-\frac{E_a + \Delta G^*}{RT}\right) \tag{4}$$

where the nucleation formation rate depends on the pathway, c is the corresponding density of nucleation sites, τ is the characteristic timescale, E_a is the activation energy including the driven forces from both strain (E_{strain}) and diffusion ($E_{diffusion}$), and ΔG^* is the critical Gibbs free energy of the nucleus at the particle size contents of three parts:

$$\Delta G^* = \Delta G^*_{bulk} + \Delta G^*_{interface} + \Delta G^*_{surface} \tag{5}$$

where the free energy at the interface and surface contribute to the tension (γ) and area (S), i.e.

$$\Delta G^*_{interface} = \gamma_{interface} S^*_{interface} \tag{6}$$

$$\Delta G^*_{surface} = \gamma_{surface} S^*_{surface} \tag{7}$$

Moreover, the $E_{diffusion}$ may depend on termination during exsolution, as shown in Fig. 1c. The lattice restricts the doped cation to resist

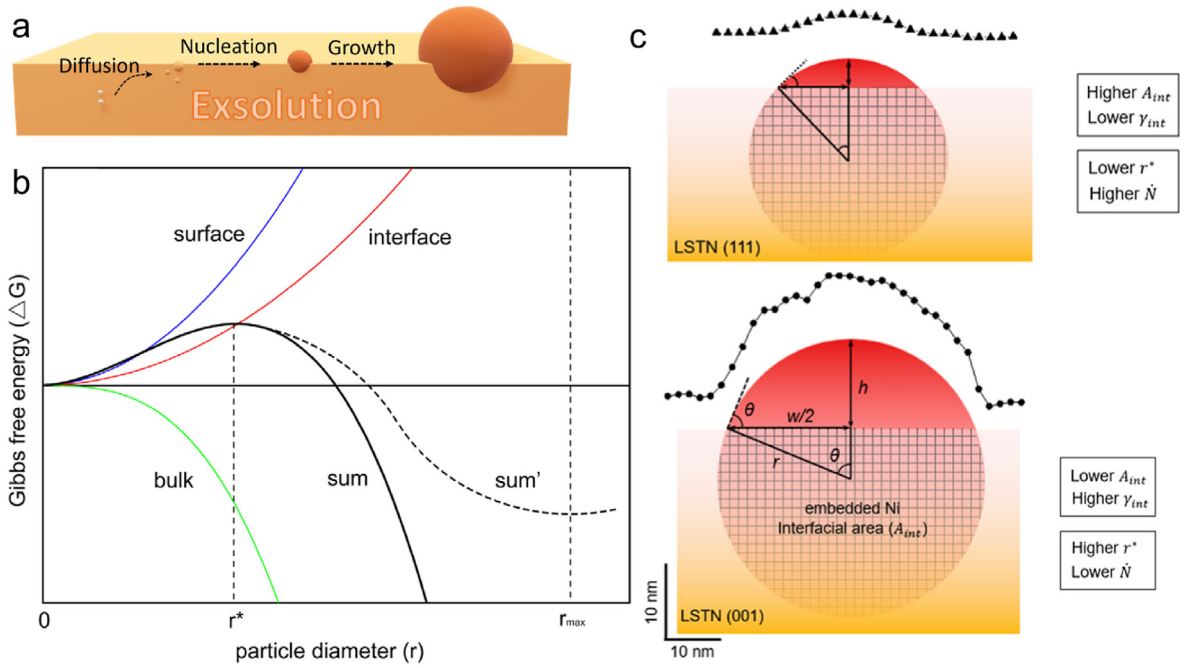

Fig. 1. (a) Illustration of the exsolution process. (b) Gibbs free energy changes during nucleation and growth. Reproduced with permission from Ref. 38. (c) Height and lateral diameter profiles (black symbol with line) of a representative exsolved particle on (111)-oriented film and (001)-oriented film. Reproduced with permission from Ref. 39.

degradation of the original structure which endows the material to resist harsh reduction[34] compared with the conventional wet chemical mixing.[35] Besides, spinodal decomposition is put forward mainly on the exsolution of noble metal by thermodynamic theory.[36,37] This can clearly and accurately explain the order of ready exsolution for Pd > Pt > Rh.

2.3. Driving force for exsolution-external and internal

The external driving force includes thermal, chemical reduction (even oxidation), electroreduction, photoreduction, and pre-decorated alien species, as shown in Fig. 2. Thermally driven without reduction is achievable for metal oxide migrating from the ceramet framework.[40] This is also common for noble metal cooperated material as the noble metal cation endure reduction at high temperature even in ambient condition.[41] Generally, chemical reduction at high temperatures is necessary to break the chemical bonding (metal-oxygen, M–O) as it is an energetic process.[42] Electrochemical reduction has been used to drive the formation of metal near the surface.[43,44] Cathodic polarization offers a fast kinetic effect that produces fine nanoparticles in a short time. Recently, photo-reduction was examined to transfer the electrons to local sites, which activates the ingress of metal particles.[45] The N_2 plasma was applied to trigger the exsolution of Ni particle by forming an electron accumulation layer.[46] It is even possible to drive the emergence of nanoparticles at room temperature under the ion bombardment of an argon low-pressure plasma.[47] Thus, more possible ways to trigger the exsolution could be explored.

To assist the separation of cations on B-sites, introducing A-site deficiency was utilized in different materials. Non-stoichiometry plays a pivotal role in fabricating the exsolution system.[23,48] Designed non-stoichiometry materials were reported to form more uniform nanoparticles, including single metals and alloys.[49] Besides, lattice strains tune the size and population of exsolved nanoparticles on thin film.[50]

2.4. Types of exsolved nanoparticles

The review of exsolved metallic particles can be categorized based on the elemental blocks. Alkaline earth metal, especially strontium oxide

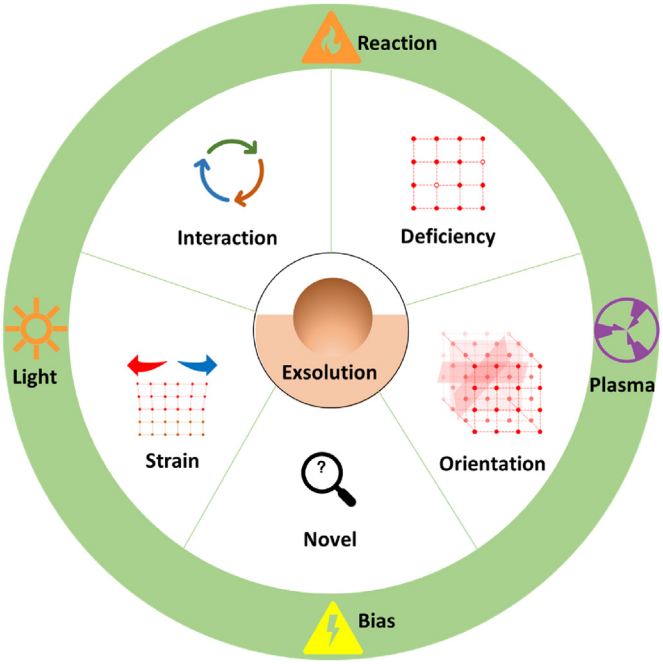

Fig. 2. Outer: driving forces to trigger the exsolution in materials: chemical reactions, biasing, plasma, light. Inside: approaches to tune the exsolution: defective chemistry, strain, interaction.

has been extensively studied as a certain type of exsolution that occurs when the secondary phase is formed during treatment under oxidation.[51] Though it can negatively impact charge transfer and material performance, it can be beneficial if precise control can be achieved. Exsolved B-site metal particles are known to provide catalytic performance and have garnered significant attention in the catalytic field. In the following sections, we will review the different types of metallic particles that can be exsolved on materials.

2.4.1. Noble metals

The regenerated Pd nanoparticles were the first report on $LaFe_{0.57}Co_{0.38}Pd_{0.05}O_3$ by Y. Nishihata et al. as a 'smart' catalyst.[52] The size of Pd maintained ranges from 1 to 3 nm even after aging in the engine exhaust gas at 900 °C for 100 h. Noble metals including Au[28] Ag[53,54] Pt[55] Rh[56] Ru[57,58] and Ir[59] have been reported in numerous systems and utilized for renewable energy and catalytic applications. The diffusion of cations is limited by the ionic radius and the ionic charge. The larger noble metal cations are normally hard to diffuse to the surface of the host but are trapped in the matrix of the host material.[60]

2.4.2. First-row transition metals

The exsolution of first-row transition metal flourishing after introducing the non-stoichiometry to facilitate the exsolving of nanoparticles.[23] Exsolution started to receive increasing attention when its capability was further expanded to first-row transition metals, such as Ni[23] Co[61] Cu[62] and Fe.[63] The exsolved bimetallic nanoparticles also exhibit promising synergic effects in various applications.[64,65] The catalysts with decorated bimetallic nanoparticles (for example, CoFe[66,67] and NiFe[68,69]) show significant performance improvement due to the synergic effect. The generation of core-shell rather than bimetallic particles relies on the mixing enthalpy conditions.[70] Trimetallic are proved to be more active than single or bimetallic catalysts. Tatsumi Ishihara et al. demonstrate the possibility of forming Cu–Ni–Fe alloy matrix by in-situ decomposing spinel oxides of $Cu(Ni)Fe_2O_4$ in a reduction atmosphere.[71] Ternary Ni–Co–Fe alloy formed on the A-site deficit perovskite $Sr_{0.93}(Ti_{0.3}Fe_{0.56}Ni_{0.07}Co_{0.07})O_{3-\delta}$ and double perovskites has been reported to improve the performance of the SOFC[72] and dry-reforming of methane.[73]

2.4.3. Other potential candidates for exsolution

Exsolution of other transition metals such as W[45] and Ce[74] have also been investigated. The metallic elements in the P block posse high electronegativity and stable valence and serve no exsolution-like phenomenon. However, it has been found that the oxide particles formed if excess Bi-doped on the A-site while a detailed investigation is necessary to confirm the separation of this phase.[75] The decorated particles can be reformed by post-treatment, such as sulphuration,[45] phosphatisation,[76] or hydroxy absorption.[77]

It is, therefore, reasonable to introduce exsolution as a promising method to produce multi-element nanoparticles. By tuning the thermodynamic parameter, the production of poly-elemental nanoparticles with multiple-interface architectures may also be possible. All those conceptions depend on a well understanding of exsolution and encourage the discovery of further mechanism underpinning.

2.5. Applicable host material

A broad range of host materials will be studied to get insight into the relationship between exsolution and the parent material composition. Exsolution attracted much attention by widely investigating enriching host materials, including perovskite, spinel, and other materials.[78]

Titanates as popular host materials were reviewed to understand the specific phenomenon. The prototype perovskite $SrTiO_3$ has been widely studied based on various doping strategies.[79] As the most common system, A-site doped strontium titanates demonstrate interesting properties.[80] The acidity of titanium superior to scandium and zirconium improves the hydrogen evolution reaction activity of the heterogeneous catalysts.[77] Metal-doped chromates[81–83] and ferrite-based[68,84,85] perovskites were widely investigated in the exsolution field. Nanoparticles exsolved on other perovskites have also been reported, including double perovskites Ni-doped $(Pr_{0.5}Ba_{0.5})_{1-x}MnO_5$,[86] Ruddlesden-Popper (RP) perovskite[87–89] and hexagonal perovskite $Ba_8Ta_6NiO_{24}$.[90]

Not limited to the perovskite, recognized oxides such as ceria and zirconia have also been utilized as hosts for exsolution.[91] Phase separation refers to extended exsolution reported on various solid solutions, such as NiO–MgO,[92] NiO–CeO_2,[93] Pyrochlore $La_2Z_2rO_7$[94] and Fluorite type $Sm_2Ce_2O_7$.[95]

Limited by the reservation of cation, the exsolution has been widely reported on pellet/particle host and thin-film materials because of the successive cation supply. The support size is essential to be more significant enough to provide enough cations for the growth of the nanoparticles.[78] The particular host material smaller than 1 μm demonstrates a lower population of exsolved nanoparticles (except with the exsolution of high percentage host cations[96]). As changing the morphology of the support, the physicochemical role varied in determining the exsolution process. The diffusion depth of cations/vacancies during reduction for perovskites seems limited to 200 nm.[97] In the thin film-based exsolution, the surface nucleation would be predominated than the diffusion since the travel distances would be shortened. The thin film has been utilized to study the strain effect because of the facile modulated lattice strain.[50,98] Moreover, the thin film support generally exhibits controllable termination, which may lead to preferential segregation of exsolved nanoparticles.[39]

Although the loose powder (with a size below a micrometer) may adhere to similar exsolution fundamental as a thin film, the small cation stock limited by the volume restricts the exsolution proceedings. From this point of view, the exsolution of powder-like structure was reported only on considerable dopants rather than little dopants.[99] A one-dimensional continuous structure, i.e. fibers should be promising for the diffusion of cations, thus, worthy to be used to investigate the exsolution. $PrBa_{0.5}Sr_{0.5}Co_{0.2}Fe_{1.8}O_{5+\delta}$ nanotubes decorated with cobalt were produced by thermal reduction. They promote the performance of soot combustion compared with bulk-based catalysts.[100] The interval fiber structure opens a way for easier transportation of solid carbon and intact contact between catalysts and soot particles. Ni nanoparticles exsolved on $La_{0.3}Sr_{0.6}Ni_{0.1}Ti_{0.9}O_3$ fiber calcined at 800 °C were reported.[101] The continuous fiber structure offers a pathway for the transition of cation diffusion which is proved by the higher population of nanoparticles on the thin fiber area.

3. Fundamentals of CO_2 reduction in SOECs

CO_2 SOECs are solid-state electrochemical devices that convert CO_2 to CO or CO_2-steam to produce syngas (CO and H_2). The high-value fuel products and the oxygen produced on the opposite side are precursors for industrial utilization. Based on the highly efficient SOECs, a closed cycle that achieves carbon capture and utilization could be built up.

3.1. Thermodynamics of CO_2 reduction

Thermodynamics determines reaction directions, equilibriums of reactions and minimum energy required to sustain electrochemical reactions. The thermodynamic process is important to understand the performance of CO_2 solid oxide electrolysis cells (SOECs). Herein, the thermodynamics of solid oxide electrolysis cells will be studied together as the solid oxide cell system can be utilized in a reversible model. SOEC as a candidate to produce value fuels has been investigated for CO_2 emission control. CO_2 electrolysis involves reducing CO_2 to CO and oxide anions (or combining with hydrogen to synthesize high-value products) on the fuel electrode. The oxide ion-conducting SOEC can directly electrolyze CO_2 into CO and oxygen under externally applied potential. CO_2 is adsorbed on the surface of the fuel side electrode (cathode in SOEC) and split into CO and O^{2-}. The O^{2-} will transport to the air side through the electrolyte. The reaction of CO_2 electrolysis on the cathode can be written as follows:

$$CO_2 + \text{electric energy}\ (\Delta G) + \text{heat}\ (T\Delta S) \rightarrow CO + \frac{1}{2}O_2 \quad (8)$$

The energy demand as a function of operating temperature for CO_2 electrolysis is shown in Fig. 3a (by HSC Chemistry software). ΔH (the enthalpy change), ΔG (the Gibbs free energy change) and $T\Delta S$ (T:

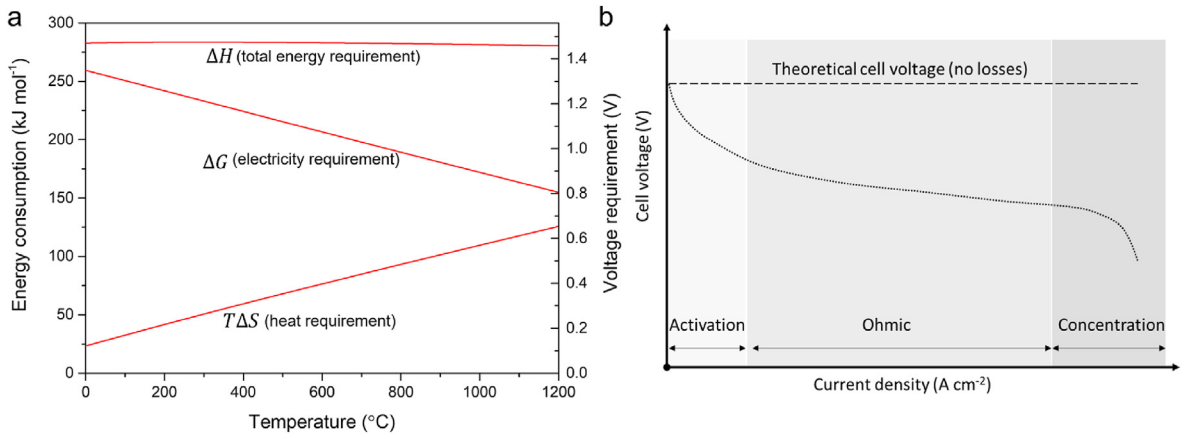

Fig. 3. (a) Thermodynamics of CO_2 electrolysis. (b) Schematic of fuel cell *I–V* curve. In contrast to the theoretical thermodynamically predicted voltage (dashed line) and the actual voltage of a fuel cell (dotted line) due to unavoidable losses in the cell. Reproduced with permission from Ref. 104.

temperature; ΔS: the entropy change) are the demands of total energy, electrical energy and heat, respectively. With increasing temperature, the required electrical energy for SOEC decreases and the thermal energy demand increases. Therefore, the heat supplied by the operating environment or other thermal energy (for instance, nuclear reactor) can compensate for the less electrical energy demand for the electrolysis. While low-temperature electrolysis techniques face some crucial problems, including lean reaction kinetics (low CO_2 solubility in the aqueous electrolyte), catalyst degradation, and low selectivity.[102,103] SOEC offers a promising way to tackle those problems under high temperature (700–1000 °C). The high temperature will improve the kinetics of reactions in SOECs, and in turn enhance the performance. Moreover, the required heat of the electrolysis process can be obtained from joule heat in the cell.

3.2. Reaction kinetic of CO_2 reduction

Thermodynamics govern the electrochemical reactions in SOECs, whereas kinetics dominates the reaction rates of SOECs. The electrolysis of CO_2 can be slow due to the limited kinetics even when cell voltages are higher than the reversible potentials (thermodynamical available).

As the cell is connected to a complete circuit with loads or power supply, the current flows in the circuit, indicating the cell is in operation. The performance of a cell under operation is determined by many factors, such as the materials (reactivity, conductivity, thermal expansion coefficient), fuel contamination, redox stability and microstructure (thickness, porosity). There are losses present in the cell that cause the cell system to be irreversible. The practical performance is always lower than the ideal condition, as shown in Fig. 3b, due to three major cell losses (also referred to the polarization, represented as η) that exist during the operating, including activation loss, ohmic loss and concentration loss, leading to an actual operating voltage as:

$$E = E_0 - (\eta_{act} + \eta_{ohm} + \eta_{conc}) \quad (9)$$

The voltage dropping at the low current density (especially for low-temperature fuel cells) is responsible for the activation losses. At this stage, the electronic barriers need to be overcome before ionic transport. Though increasing the temperature may lead to an enhancement of electrode kinetics, the key is the activity of the electrode material itself. The exsolved materials are attractive due to the abundant metallic nanoparticles that act as active sites for the reaction.

The ohmic losses are governed by material selection, operating temperature and thickness of the components (or path for current) relay on the electronic resistance of electrodes and ionic resistance of electrolytes. The electrodes typically have high electronic conductivity, especially, an improvement was achieved for the exsolved materials under reduction.[105] Thus the contribution of ohmic losses for the electrodes was relegated or even neglected. Therefore, minimizing the thickness of electrolytes while ensuring gas tightness is crucial for building up a high-performance fuel cell. Besides, the contact resistance should be considered as a contributor to the ohmic losses.

The concentration losses are also known as mass/gas transport polarization caused by reactant depletion and concentration gradient. The losses occur mainly due to diffusion problems in the system, including not fluent circulation of reactants into electrode pores and the slow dissolution of products out of reactive sites. A specific porosity of electrodes or tailored microstructure allows electrodes to reduce cell losses during the operation.[106,107]

3.3. CO_2 reaction mechanisms on exsolved materials

Taking the advantage of using renewable electricity resources, the CO_2 electrolysis cell transfer the industrial waste CO_2 into CO and oxygen. Both products can be utilized as feedstock for other applications, as illustrated in Fig. 4. The CO_2 electrochemical reduction mechanism were widely studied mainly on the low temperature transformation techniques.[108] The theoretical studies on high temperature CO_2 reduction were focused on the effects of the oxygen vacancies, for example the adsorption of CO_2, and the activation effect of nanoparticles on the supports. The high-temperature electrochemical reduction of CO_2

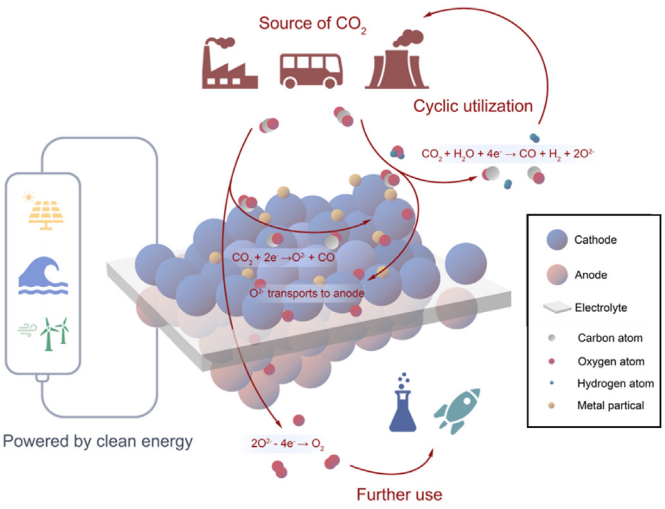

Fig. 4. Schematic diagram of CO_2 electrolysis using a solid oxide cell for syngas and O_2 production.

contains two half-reactions: CO_2 reduction at the cathode and oxygen evolution reaction at the anode. As the former is the main topic in this work, we will focus on the elementary steps in CO_2 electrochemical reduction.

Based on the Ni-based electrodes, Shi et al. proposed four elementary steps mechanism for CO_2 electrolysis in Ni/YSZ electrode, including CO_2 adsorption, CO_2 decomposition, surface diffusion of O(Ni) and charge transfer reaction at the TPB and desorption.[109] Similarly, it is consensus that the CO_2 firstly adsorbed on mixed ionic and electronic conductors (MIECs) to form carbonate. The adsorbed carbonate species then decompose into CO and oxygen ion, subsequent to the desorption of CO and transfer the oxygen ion to the anode. However, it is still ambiguous about the CO_2 reduction mechanism in the SOECs, especially the adsorbed sites on the cathode surface.[110]

The oxygen vacancy plays a key role in the adsorption of CO_2, specific the bonding configuration and the intermediates.[111] The adsorbed CO_2 molecule presents in a bidentate configuration with carbon atom on lattice oxygen and A-site cation. The configuration shows an larger initial O–C–O angle (171.47°), which decreased to 124.94° as carbonates intermediates formed. The angle increased again through the exchange between oxygen and vacancy at the surface, left with linear CO adsorbed on B-site atom. This dissociative adsorption of CO_2 process had a highest energy barrier among the reduction pathway and was the rate-limiting step.[112] In comparsion, the followed CO_2 desorbtion and oxygen integration are easy to proceed under the SOEC operating conditions.

The calculation results show that the presence of oxygen vacancies on the catalyst surface can reduced the adsorption energy of CO_2 compared with stoichiometric surface.[113] The B-site cation seems affect the adsorption of CO_2 as well, illustrated with diffuse reflectance infrared Fourier transform (DRIFT) spectra. The oxygen affinity and activation energy of B-site dopants tune the reduction reaction process. In the Ni and Mn doped (La,Sr)FeO_3, the Mn prefers to bind with oxygen while Ni is more favor to bind with carbon in the CO_2, therefore, the Ni–Mn co-doping perform lower free energy of the CO_2 electrolysis process.[114]

Exsolved materials typically present an ionic conductivity due to the high concentration of oxygen vacancies. Most of the exsolved species are host in the B-site in oxides lattice and hybridized with the surrounding oxygen ions in octahedral.[115] It is therefore responsible for the catalytic activity and electron transfer. In the case of CO_2 reduction, the cations in B-site coupled with oxygen vacancies to promote the adsorption and activation of gas molecules.[21,116] A reasonable reaction step for CO_2 electrolysis for mixed ionic-electronic conductor exsolved materials according to the calculation results, may involve both pathways. Most likely, the CO_2 adsorbed at the interface of metal-oxide support, as shown in Fig. 5a. Theoretical studies reveal that CO_2 adsorbed at the interface between metal and support oxide with linear O–C–O angle bent od an angle during the transition state.[18,111,117] The CO_2 molecular activation and oxygen migration are important to understand the CO_2 reduction process on exsolved material. The potential energy diagram of the CO_2 activation process was calculated to provide insights into the reaction, as shown in Fig. 5b. The calculation result indicates that exsolved nanoparticles can initiate CO_2 activation, and improve CO desorption.

4. Materials for fuel electrode in CO_2 SOECs

The three main components in SOECs are air electrodes, electrolytes and fuel electrodes. Their functions determine various requirements for the materials used in SOECs such as chemical and mechanical compatibility of components, good conductivity, high activity, etc. Here, the materials employed in solid oxide cells were reviewed together, with specific highlights if needed.

4.1. Air electrode

The air electrode refers to the electrode exposed to air/oxygen, i.e. cathode in SOFC or anode in SOEC. On this side, the O_2 is dissociated into oxide anions. Thus, high electrocatalytic activity towards this process is in high demand. The air electrode must possess sufficient electron conductivity to accomplish this reaction. Besides, CO_2 tolerance is needed if the electrode is exposed to air rather than pure oxygen. It has been found that the kinetics of oxygen reduction reaction (ORR) may restrict the electrochemical effectiveness.[118] Therefore, a better air electrode is crucial to obtain an advanced fuel cell. Platinum has been used as an air electrode to investigate the chemical and electrochemical steps on electrodes but not for practical utilization.[119] As an alternative, MIECs are widely used as air electrodes, such as manganite (Ca[120] and Sr[121] doped $LaMnO_3$, $SmBaMn_2O_{5-\delta}$[122]), cobaltite and ferrite ($LaCoO_3$,[123,124] $Ba_{1-x}Sr_xFeCoO_3$,[125] $SmBaCo_2O_{5-\delta}$[126]) and nickelate ($La_{n+1}Ni_nO_{3n+1}$[127]).

4.2. Electrolyte

The electrolyte is made dense to avoid gases crossover, which causes fuel leaking and wastage. An adequately high ionic conductivity ensures the migration of ions (proton or oxide anion) through electrolytes while

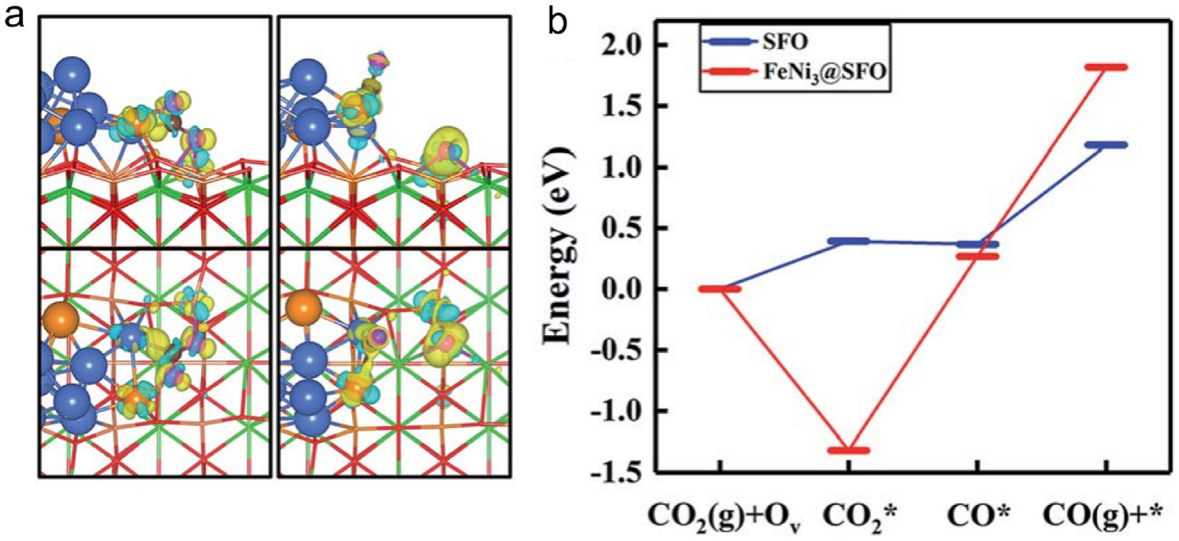

Fig. 5. Theoretical calculations Schematic of CO_2 reaction in exsolved electrode. (a) Charge density difference isosurface for CO_2 and CO configurations over exsolved FeNi/$SrFeO_3$. (b) Potential energy diagram of CO_2 reduction over $SrFeO_3$ surface and FeNi/$SrFeO_3$ interface. Reproduced with permission from Ref. 117.

the electrons travel on electrodes and the loaded circuit. The electrolyte type can be functionally categorized as the oxide ionic conductor or proton conductor. The electrolyte can also be sorted based on the operating temperature, including high, intermediate and low-temperature electrolytes. To date, the most widely employed electrolyte oxide ionic conductor includes stabilized zirconia, doped ceria and doped lanthanum gallate.[128] Zirconia-based fluorites, the ternary zirconia (with CaO, MgO, Y_2O_3 and Sc_2O_3 doped), are commonly used in solid oxide cells.[129] The application of zirconia is limited at high temperatures as its conductivity falls at lower temperatures. $Ce_{1-x}Gd_xO_2$ and $Er_{1-x}Bi_xO_3$ demonstrate superior chemical stability with various electrodes and high ionic conductivity even at low temperatures.[130] The disadvantage of this electrolyte is the inferior stability in low oxygen partial pressure (high electronic conductivity), which causes short-circuiting during operation. Perovskite-structured oxides are promising because of their high ionic conductivity. The most well-studied perovskite electrolyte is the (Sr and Mg)-doped $LaGaO_3$.[131] However, the development of doped $LaGaO_3$ was hampered by serval factors, such as difficulty in obtaining pure phases, volatility of gallium at high temperatures, and poor compatibility with Ni-based electrodes. Building on ceria and bismuth oxides, electrolytes that suit low temperatures have been developed.[132]

4.3. Fuel electrode

The fuel electrode is exposed to the fuel environment and converted the fuels into oxidation products with oxide ions transported through the electrolyte. The fuel electrode materials must possess sufficient catalytic activity, high electronic conductivity, coking tolerance and a long lifespan during operation.[133]

Ni-YSZ cermet is currently the favored fuel side electrode material to achieve most requirements.[118] The advantage of this composite is its superior performance with hydrogen fuel coupled with its good current collection, leading to a low electrode resistance. NiO-YSZ porous framework is easily fabricated by calcination in the air, followed by in-situ reductions. Ni couples with ionic conducting YSZ in the composite to offer electronic conducting and catalytic activity for fuels. Mixed YSZ provides thermal expansion buffering for nickel metal with a well-matched thermal expansion coefficient (TEC) with electrolyte.[134] This mixture phase together with the gas phase formed TPB as active sites for the transfer of the electrons, oxygen ions and gas molecules. Increasing the TPB in the electrode is therefore crucial to improve the fuel cell performance because of offering more reacting sites. Several weaknesses restrict the broad applicability of Ni/YSZ electrodes, such as coking,[135] sulfur poisoning[136] and redox instability due to fuel starvation (through lack of fuel, on shut-down or under high current density for electrolysis). Ni/YSZ in redox experiences volume changing and coarsening, leading to activation degradation and performance decrease. Stemming from the Ni-YSZ concept, electrode materials formed by mixing metallic catalysts and ionic conductors were developed, such as electrodes based on Ni alloys,[137–139] Cu–$CeO_{2-\delta}$,[140] and other catalysts.[141,142]

The state-of-art materials for solid oxide cells are single-phase mixed ion and electron conductors (MIECs). As alternative electrodes, MIEC materials are redox-stable, ideally providing more reaction sites (all the surfaces in contact with the gas phase). The advanced MIEC materials are widely investigated as fuel electrodes for solid oxide cells.

Doped pyrochlore systems exhibit both ionic and electronic conductivity, while the stability of the phases in reducing atmosphere was non-adequate for application.[143] The most explored and exciting composition recently is perovskite which exhibits programable properties with flexible structural tolerance.[115] The perovskite oxides exhibit good thermal and mechanical stability and chemical compatibility with electrolytes. Most importantly, a wide range of properties can be tailored by altering A and B-site cations in perovskite. The multiple oxidation states of these cations enable the creation of oxygen vacancies by doping and may give rise to electronic conductivity under reducing conditions.

Moreover, the active redox couple on B-site provides the active sites for gas dissociation and adsorption on the electrode surface. Cr, V and Ti, are commonly employed to avoid the collapse of the structure under reducing conditions and have been frequently studied using doping strategies.[22,144] Recently, most of the perovskites studied stemmed from chromites ($LaCrO_3$) and titanates ($SrTiO_3$). In addition to conventional Ni-based material, cermet electrodes present salient performance. The stability of $La_{0.75}Sr_{0.25}Cr_{0.5}Mn_{0.5}O_{3-\delta}$ in both oxidizing and reducing environments endows it as a candidate electrode for CO_2 electrolysis.[145] The titanate-based perovskites also possess superior redox stability and n-type conductivity under strong reducing conditions as cathodes in the electrolysis mode.[18,146] Strategies in the search for promise materials focus on metal decoration (impregnation and exsolution) and functional engineering (surface defect and vacancy construction).

5. Exsolved material in CO_2 reduction

The fuel electrode plays a crucial role in CO_2 electrochemical reduction, thus has been widely investigated as seen from the above-mentioned overview of CO_2 reduction fundamentals. Among various fuel electrodes, electrodes decorated with exsolved particles demonstrate more promising performance than bare composition and even those with infiltrated active sites.[21,22,147] Here, we summarize the literature published so far in this area with synthesis methods, types of exsolved metal and structure of support, as shown in Fig. 6. The solid-state mothed was the most used to prepare pure oxide electrode materials, followed with sol-gel which provide smaller size samples with more active site. The exsolution as a state-of-the-art method starts to attract much attention with extended kinds of material systems in CO_2 reduction applications, such as perovskites, fluorite and spinel. The performance of the CO_2 electrolyzer with exsolved materials was summarized in Table 1.

5.1. Types of exsolved metal particles

5.1.1. Electrode with single metal particles

It is widely accepted that the exsolved metallic nanoparticles provide active sites for catalytic reactions.[165] The exsolved noble nanoparticles such as Rh,[163] Ru[182] attract attention for CO_2 electrochemical reduction. The transition metals and their alloy were widely investigated to reduce the usage of noble metals, as shown in Fig. 7a. Beyond the type of metals, some other factors can be catalogued to understand the possible reason

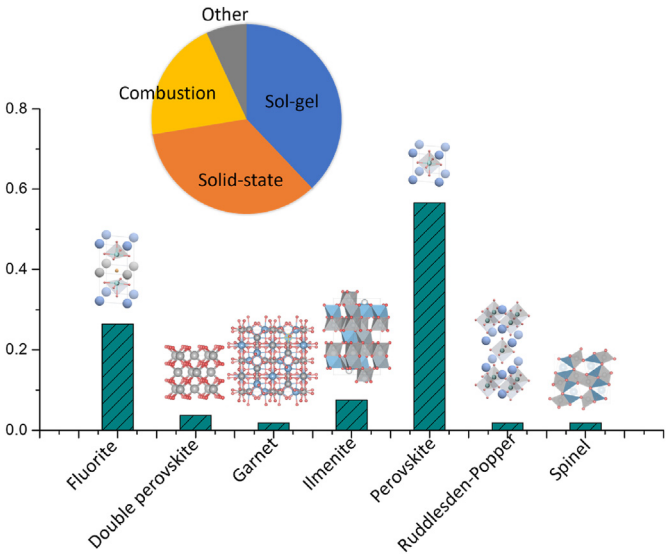

Fig. 6. Exsolution infographic on CO_2 electrolysis. Statistical analysis on about 60 papers published in the field of CO_2 electrolysis since 2014. Including the structure of the exsolved material system and synthesis methods.

Table 1
Performance for high temperature CO_2 electrolysis with exsolution cathodes.

Cathode material	Feeding gas	R_p(Ω cm^2)/Volt. (V)/Temp.(°C)	Current density (A cm^{-2})/Volt.(V)/Temp.(°C)	Ref.
$(La_{0.75}Sr_{0.25})_{0.9}(Cr_{0.5}Mn_{0.5})_{0.9}Cu_{0.1}O_{3-\delta}$	CO_2	0.50/1.8/800	0.25/1.5/800	148
$Ce_{0.85}Ni_{0.15}O_2$	CO_2	0.38/2.0/800	0.25/1.6/800	149
$NbTi_{0.5}(Ni_{0.75}Cu_{0.25})_{0.5}O_4$	CO_2	6.21/1.4/800	0.11/1.6/800	150
$NbTi_{0.5}Ni_{0.5}O_4$	CO_2	1.25/2.0/800	0.16/1.5/800	151
$(La_{0.2}Sr_{0.8})_{0.9}(Ti_{0.9}Mn_{0.1})_{0.9}Ni_{0.1}O_{3-\delta}$	CO_2	3.50/1.6/800	0.08/1.5/800	152
$Ni_{0.9}TiO_3$	CO_2	1.70/-/800	0.16/1.6/800	153
$(La_{0.75}Sr_{0.25})_{0.9}(Cr_{0.5}Mn_{0.5})_{0.9}Ni_{0.1}O_{3-\delta}$	CO_2	0.65/2.0/800	0.19/1.5/800	154
Ni–Fe–La(Sr)Fe(Mn)O_3	50%CO_2–1%CO–49%Ar	2.33/-/800	2.32/1.6/800	155
$La_{0.6}Sr_{0.4}Fe_{0.8}Ni_{0.2}O_{3-\delta}$	70%CO_2–30%CO	1.08/-/800	0.70/1.6/800	68
$(La_{0.3}Sr_{0.7})_{0.9}Ti_{0.95}Ni_{0.05}O_{3-\delta}$	CO_2	0.80/1.6/800	0.19/1.6/800	156
$Pr_{0.4}Sr_{0.6}Co_{0.2}Fe_{0.7}Mo_{0.1}O_{3-\delta}$	70%CO_2–30%CO	0.455/1.6/850	1.01/1.6/850	157
(La,Sr)$TiO_{3+\delta}$	30%CO/CO_2–20%H_2/N_2	0.33/1.7/800	0.79/1.7/800	158
$Sr_{1.9}Fe_{1.5}Mo_{0.4}Ni_{0.1}O_{6-\delta}$	CO_2	0.265/-/800	2.16/1.5/800	69
$SrFeO_{3-\delta}$-10%Ni	CO_2	0.37/1.6/800	0.75/1.6/800	159
$La_{1.2}Sr_{0.8}Co_{0.4}Mn_{0.6}O_4$	70%CO_2–30%CO	1.5/-/800	0.63/1.3/800	89
$La_{0.6}Sr_{0.4}Fe_{0.8}Ni_{0.2}O_{3-\delta}$	CO_2	0.12/1.6/800	0.60/1.6/800	160
$Sr_2Fe_{1.5}Mo_{0.5}O_{6-\delta}$	95%CO_2–5%N_2	0.20/1.6/800	0.93/1.6/800	117
Ni/$Cr_2O_{3-\delta}$	CO_2	0.08/1.6/800	2.07/1.6/800	161
$NbTi_{0.4}Cr_{0.1}Ni_{0.5}O_4$	80%CO_2–2%CO–Ar	0.22/1.6/800	1.6/1.6/800	162
$La_{0.43}Ca_{0.37}Rh_{0.06}Ti_{0.94}O_3$	25%CO_2–25%H_2O–50%N_2	0.21/-/850	1.57/1.0/850	163
$Sr_2Fe_{1.45}Ni_{0.05}Mo_{0.5}O_{6-\delta}$	CO_2	0.87/1.0/800	0.73/1.5/800	164
$La_{0.43}Ca_{0.37}Ni_{0.06}Ti_{0.94}O_3$	25%H_2O–25%CO_2–50%H_2	0.73/-/850	1.10/1.6/850	165
$Sr_2Fe_{1.3}Co_{0.2}Mo_{0.5}O_{6-\delta}$	50%CO_2–50%CO	0.60/OCV/800	1.34/1.4/800	166
$(Pr,Ba)_2Mn_{1.82}Fe_{0.18}O_{5+\delta}$	CO_2	1.00/1.6/850	0.64/1.6/850	167
$Sr_2FeMo_{0.55}Co_{0.45}O_{6-\delta}$	CO_2	0.12/1.5/800	2.00/1.5/800	168
$(La_{0.65}Sr_{0.3}Ce_{0.05})_{0.9}(Cr_{0.5}Fe_{0.5})_{0.85}Ni_{0.15}O_{3-\delta}$	CO_2	0.23/1.2/800	1.78/1.6/850	169
$(La_{0.2}Sr_{0.8})_{0.85}Ti_{0.8}Cr_{0.1}Ni_{0.1}O_{3-\delta}$	CO_2	0.43/1.6/850	0.80/1.6/850	170
$La_{0.4}Sr_{0.6}Co_{0.2}Fe_{0.7}Mo_{0.1}O_{3-\delta}$	95%CO_2–5%N_2	0.08/1.6/800	1.45/1.6/800	171
$Sr_2Fe_{1.35}Mo_{0.45}Co_{0.2}O_{6-\delta}$	95%CO_2–5%N_2	0.12/-/800	1.20/1.6/800	172
$La_{0.66}Ti_{0.8}Fe_{0.2}O_{3-\delta}$	20%CO_2–80%CO	0.16/1.4/800	0.80/1.4/800	146
$La_{0.6}Sr_{0.4}Co_{0.5}Ni_{0.2}Mn_{0.3}O_3$	70%CO_2–30%CO	0.85/-/800	0.79/1.5/800	173
$Gd_3Fe_5O_{12}$	CO_2	0.11/1.6/800	1.62/1.6/800	174
$La_{0.5}Sr_{0.5}FeO_{3-\delta}$	CO_2	0.25/1.0/800	1.22/1.5/800	175
$La_{0.6}Sr_{0.4}Mn_{0.2}Fe_{0.8}O_{3-\delta}$	70%CO_2–30%CO	0.33/OCV/800	1.43/1.5/800	176
$Sr_2Fe_{1.4}Ru_{0.1}Mo_{0.5}O_{6-\delta}$	CO_2	0.11/1.2/800	1.30/1.6/800	177
$Sr_2Fe_{1.25}Cu_{0.25}Mo_{0.5}O_{6-\sigma}$	50% CO_2–50% CO	0.81/-/800	2.50/1.5/800(CO_2)	178
$(La_{0.2}Sr_{0.8})_{0.9}Ti_{0.5}Mn_{0.4}Cu_{0.1}O_{3-\delta}$	CO_2	0.30/OCV/800	1.95/1.6/800	179
$La_{0.55}Sr_{0.45}Fe_{0.85}Mo_{0.15}O_3$	CO_2	0.14/1.6/800	1.15/1.4/800	180
$Sr_{1.95}Fe_{1.4}Sn_{0.1}Mo_{0.5}O_{6-\delta}$	CO_2	0.15/1.8/800	3.27/1.8/800	181
$Pr_{0.4}Sr_{0.6}Fe_{0.8}Ru_{0.1}Mo_{0.1}O_{3-\delta}$	CO_2	0.32/1.4/800	0.83/1.4/800	182
$La_{0.6}Sr_{0.4}Ni_{0.2}Fe_{0.75}Mo_{0.05}O_{3-\delta}$	CO_2	0.80/1.5/800	0.59/1.5/800	183
$La_{0.5}Sr_{0.5}Fe_{0.8}Co_{0.2}O_{3-\delta}$	95% CO_2–5% N_2	0.13/1.2/800	1.80/1.6/800	184
$Sr_{1.9}Fe_{1.5}Mo_{0.4}Ni_{0.1}O_{6-\delta}F_{0.1}$	50% CO_2–50% CO	0.31/OCV/800	2.66/1.5/800(CO_2)	185
$Pr_{0.4}Sr_{1.6}Ni_{0.2}Fe_{1.3}Mo_{0.5}O_{6-\delta}$	CO_2	0.11/1.4/800	1.58/1.4/800	186
$Sr_2Ti_{0.8}Co_{0.2}FeO_{6-\delta}$	CO_2	0.22/1.6/800	1.26/1.6/800	187
$La_{0.43}Ca_{0.37}Ti_{0.94}Ni_{0.06}O_{3-\delta}$-Ce	50% CO_2–50% CO	0.51/1.3/800	0.43/1.3/800	188
$La_{0.75}Sr_{0.2}Ca_{0.05}Cr_{0.5}Mn_{0.45}Fe_{0.05}O_3$	CO_2	1.27/1.2/800	0.60/1.6/800	189
$La_{0.75}Sr_{0.25}Cr_{0.5}Fe_{0.575}O_{3-\delta}$	CO_2	0.31/1.8/850	0.72/1.6/850	190
$Pr_{0.5}Ba_{0.5}Fe_{0.8}Ni_{0.2}O_{3-\delta}$	CO_2	0.88/1.4/800	0.84/2.0/800	191
$La_{0.75}Sr_{0.25}Cr_{0.5}Fe_{0.5}O_{3-\delta}$	CO_2	0.26/1.0/800	1.15/1.5/800	147
$Fe_{0.1}Sm_{0.1}Ce_{0.8}O_{2-\delta}$	50% CO_2–50% CO	0.34/OCV/800	1.34/1.5/800	192
$(La_{0.2}Sr_{0.8})_{0.9}(Ti_{0.9}Mn_{0.1})_{0.9}(Cu_{0.025}Ni_{0.075})O_{3-\delta}$	CO_2	0.26/1.6/800	1.61/1.6/800	193
$CaFe_2O_4$	CO_2	0.55/1.0/800	1.20/1.6/800	194
$Sr_2Fe_{1.5}Mo_{0.3}Cu_{0.2}O_{6-\delta}$	CO_2	0.55/OCV/800	1.94/1.4/800	195
$La_{0.52}Ca_{0.28}Ni_{0.04}Fe_{0.04}Ti_{0.92}O_3$	CO_2	0.60/2.1/900	0.76/1.6/900	196

for the promotion effect of utilizing exsolved materials. Hereafter, three avenues for exsolved materials that are pivotal to understanding the exsolution and their functionalities in the CO_2 electrochemical reduction process will be analyzed, including the types of exsolved nanoparticles and its effect, exsolution mechanism in SOECs and reversibility of exsolved materials. The creation of interface, alloy effect, phase transition, self-assembly, reversibility, and electrochemical switching were discussed in this part.

About half of the reported work is focused on investigating the exsolution of single metals, such as Ni, Fe and Co, as shown in Fig. 7a. In general, the SOECs with exsolved cathode display a good performance. The tabulated current densities of reported CO_2 SOECs were summarized with exsolved materials as a cathode at an applied voltage of 1.6 V and 800 °C, as shown in Fig. 7b. SOECs with monometallic Ni decorated on electrodes show slightly lower performance than Fe- and Co-based monometallic systems, which is consistent with the oxophilicity of metals from the theoretical calculation results.[110,197]

5.1.2. Alloy effect in exsolution

CO_2 reduction based on the synergic effect of alloy nanoparticles has been widely investigated. Bimetallic nanoparticles are more appealing than their monometallic counterparts, because of the synergistic effects between different metals, as shown in Fig. 7b.[198] The iron-nickel alloy exsolved from $LaFe_{0.6}Ni_{0.2}Al_{0.2}O_3$ was used for solar thermochemical CO_2-splitting with 99% conversion at 850 °C.[199] Changrong Xia et al. has found the NiFe alloy particles exsolved on the perovskite-structured $Sr_{1.9}Fe_{1.5}Mo_{0.4}Ni_{0.1}O_{6-\delta}$, achieving a current density of 2.16 A cm^{-2} at 1.5 V at 800 °C compared with 1.05 A cm^{-2} for the same composition without nanoparticles.[69] However, the amount of $SrCO_3$ increased simultaneously with the exsolution of NiFe, which suppressed the

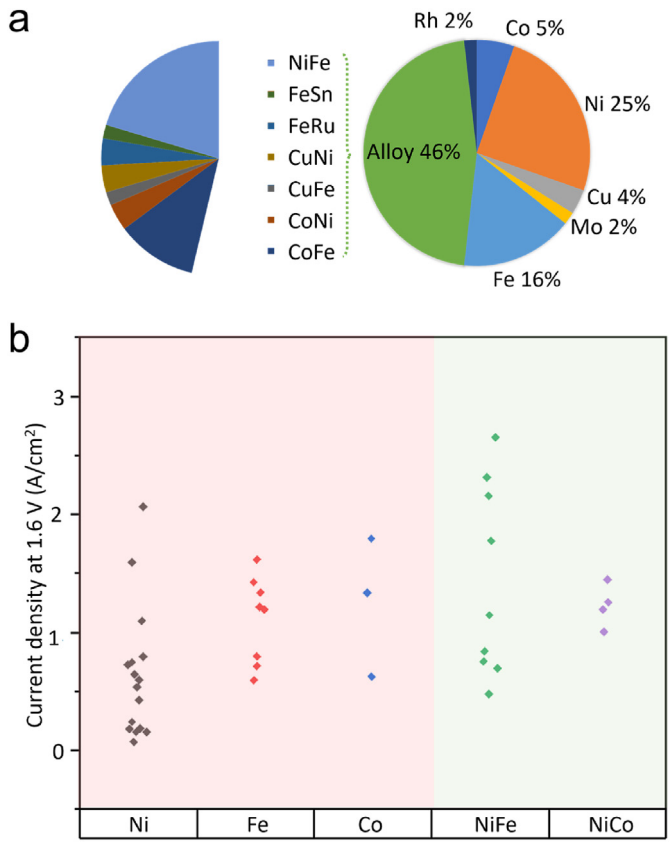

Fig. 7. Exsolution infographic on CO_2 electrolysis. Statistical analysis on about 60 papers published in the field of CO_2 electrolysis since 2014. (a) Type of exsolved nanoparticle the structure of the exsolved material system, (b) Current densities of CO_2 SOECs with exsolved materials as the electrode at an applied voltage of 1.6 V and 800 °C. Supply data in Table 1.

performance by blocking the charge transfer and diffusion of oxygenous species on the electrode surface.[164] They also developed a Ni and F co-doping strategy to achieve a promoted surface reaction rate and oxygen chemical bulk diffusion.[185] The CO_2 electrolyzer based on the synthesized oxyfluoride presents a 2.66 A cm^{-2} at 1.5 V at 800 °C.

5.1.3. Exsolved particles with heterostructure

Exoslved alloy structure exhibits high reactivity for CO_2 electroreduction, while the structure of nanoparticle attracted less attention. Control of the nanostructure of the catalyst is crucial for improving the performance of the material as it contributes to the activity of the material due to spatial and synergetic effects. The heterostructure of nanoparticles was well studied in the colloidal system, thus, it should be possible to transform the structure of particles into diversity structure by optimizing the composition of support and reaction conditions.[200] Exsolution with heterostructure nanoparticles with tuning of dopant level were also reported recently, as shown in Fig. 8.[201] The exsolved Cu seed facilitate the emergent of Fe by changing the surface energy. With increasing the iron doping amount, the heterostructure particles gradually evolved into crescent and Janus structures. The electrode with decorated Janus nanoparticles displays outstanding performance in the reversible solid oxide cel fed with H_2O/H_2 and CO/CO_2, with 1.11 A cm^{-2} at 1.3 V at 900 °C.

5.1.4. Exsolved particles with core-shell structure

It has been reported that a core-shell structure may also form during the exsolution of NiFe particles from $Pr_{0.4}Sr_{1.6}(NiFe)_{1.5}Mo_{0.5}O_{6-\delta}$.[186] FeO_x shell may form during the exsolution, as shown in Fig. 9a. The increased oxygen vacancy after reduction was evident from the XPS (Fig. 9b). The FeO_x as a shell in the particles may help to generate more oxygen vacancies and greatly enhance the kinetics of adsorption, dissociation and electrolysis of CO_2.

Tatsumi Ishihara et al. discovered the emergence of smaller particles (<200 nm) for the Ni–Fe–$La_{0.6}Sr_{0.4}Fe_{0.8}Mn_{0.2}O_3$ cathode in CO_2 electrolyzers.[155] Those Ni–Fe species significantly decrease the cathodic overpotential by increasing the active sites on the electrode. Jing-Li Luo et al. investigate the NiFe alloy exsolution on $La_{0.6}Sr_{0.4}Fe_{0.8}Ni_{0.2}O_{3-\delta}$ in CO_2 electrolysis cell, and no coking on the electrode even after 100 h stability test in CO_2 under 0.6 V at 850 °C.[68] The symmetrical cell based on this material shows a possibility of improvement by the novel structure of cells.[160] Another CoFe alloy nanoparticles were produced on Co-doped layered perovskite $(Pr_{0.4}Sr_{0.4})_3(Fe_{0.85}Mo_{0.15})_2O_7$.[157] The layer perovskite delivery more stable and efficient properties than cubic perovskite $Pr_{0.4}Sr_{0.6}Co_{0.2}Fe_{0.7}Mo_{0.1}O_{3-\delta}$ due to the promotion of oxygen vacancies. The Co dopant may decrease the segregation energy of the exsolution of iron as Co–Fe bonds have lower formation energy than the Fe–Fe bond.[29,202]

Co-doped $Sr_2Fe_{1.3}Co_{0.2}Mo_{0.5}O_{6-\delta}$ electrode also demonstrates a promising electrochemical performance with the in-situ exsolved Co nanoparticles embedded in the material.[166] Increasing the amount of Co dopants (>0.15 wt%) promotes the formation of CoFe alloy particles as well as more defects sites.[168] A hollow $La_{0.6}Sr_{0.4}Ni_{0.2}Fe_{0.75}Mo_{0.05}O_{3-\delta}$ was synthesized by molten-salt-assisted approach.[183] The exsolved $FeNi_3$ displays reversibility in the symmetrical cell based on the material electrode. The Sn-doped $Sr_{1.95}Fe_{1.4}Fe_{1.4}Sn_{0.1}Mo_{0.5}O_{6-\delta}$ exhibited promising CO_2 electrolysis performance with uniform Sn–Fe alloy particles decorated on the electrode after reduction.[181] The enhanced ability to adsorb more CO_2 on the particles may contribute to this improvement. Besides, the A-site doped $Sr_{2-x}La_xFe_{1.5}Mo_{0.5}O_{6-\delta}$ can increase the oxygen surface exchange and bulk diffusion, leading to better CO_2 electro-reduction performance.[203]

5.2. Different mechanisms of exsolution for electrodes in SOECs

5.2.1. Phase transformation in exsolved material

Co-, Mn- and Fe-based oxides may undergo phase transition under reduction condition.[191,204,205] By taking advantage of the synergetic and interfacial effect of different materials, exsolved materials as electrodes generally demonstrate high efficiency. Materials with Ruddlesden-Popper structure present a high oxygen vacancy concentration. Moreover, the exsolved metal can further decrease polarization resistance by facilitating CO_2 dissociation adsorption.[175] The phase reconstruction under reduction results to exsolution on metallic particle was correlated to the Gibbs free energy of oxygen vacancy formation.[206] With Sr dopant in $Pr_{0.5}(Ba/Sr)_{0.5}TO_{3-\delta}$ (T = Mn, Fe, Co and Ni) increasing, the oxygen vacancies are prone to form under reduction, indicating more metallic species exsolved. This phase transformation was observed in Sn-doped $Sr_{1.95}Fe_{1.5}Mo_{0.5}O_{6-\delta}$.[181] The cubic perovskite structure transformed to an Ruddlesden-Popper structure with emerged FeSn alloy nanoparticles, as shown in Fig. 10a. The phase transition has also been observed from double perovskites ($Sr_2Ti_{0.8}FeCo_{0.2}O_{6-\delta}$) to Ruddlesden-Popper structure along with CoFe nanoparticles under reduction.[187]

The reduction of $Gd_3Fe_5O_{12}$ leads to the conversion of single-phase garnet into perovskite with exsolved metallic Fe.[174] The resulting oxygen-abundant species ($GdFeO_3$ and $Ca_2Fe_2O_5$) and Fe particles promote the activation of CO_2 and electronic transfer by forming an active metal-oxide interface. Similar to the ferrates, the Co decorated Ruddlesden-Popper magnates ($La_{1.2}Sr_{0.8}Co_{0.4}Mn_{0.6}O_4$) also display a promoted CO_2 reduction activity.[89] The phase transformation was clearly evidenced by the Co K-edge and Mn K-edge X-ray absorption near-edge spectra (XANES) of Co and Mn in samples before and after reduction, as shown in Fig. 10b. The redox cycles trigger the reversibility of structural transition between perovskite and Ruddlesden-Popper for those materials which contributes to the formation of a higher concentration of

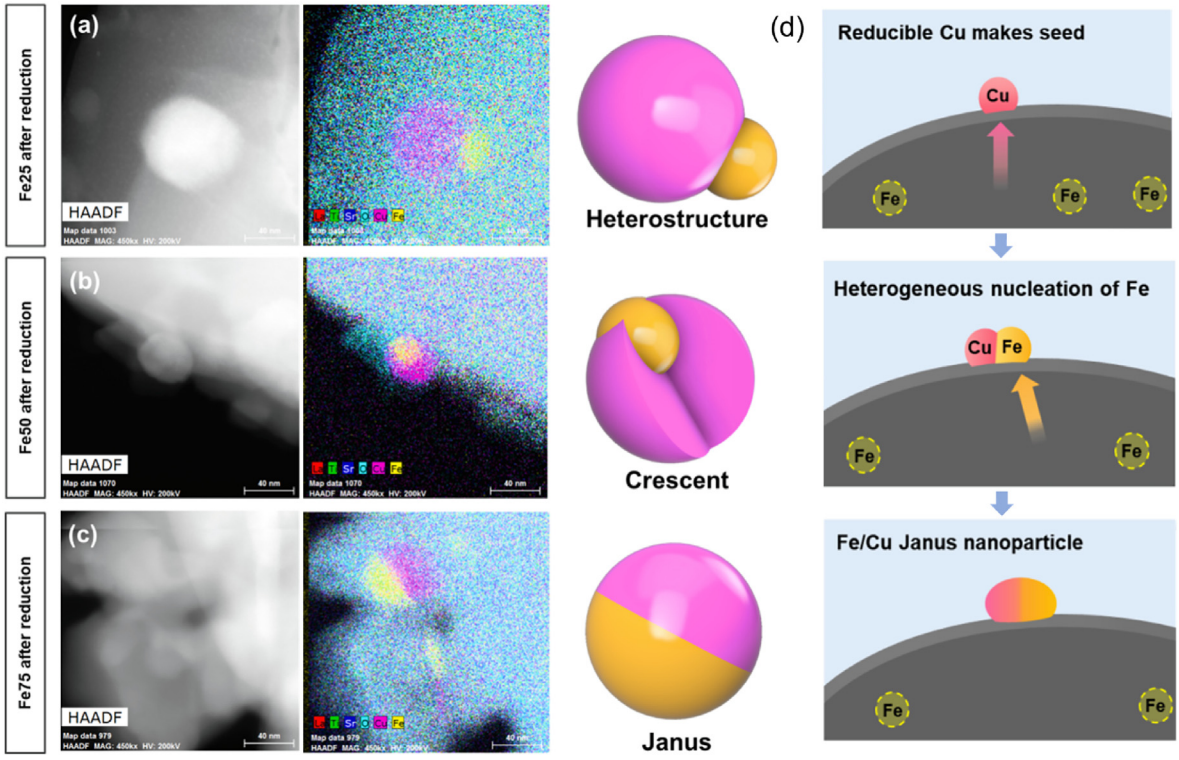

Fig. 8. Morphology of exsolved particles with heterostructure. (a–c) TEM and EDX mapping of $La_{0.43}Sr_{0.37}Fe_{0.12-x}Cu_xTi_{0.88}O_{3-\delta}$ reduced for 12 h in dry H_2. (d) Schematic illustration of co-exsolution mechanism. Reproduced with permission from Ref. 201.

oxygen vacancy. Besides, the catalyst decorated with CoNi nanoparticles shows high sulfur tolerance and activity in the CO_2 electrolysis cell.[173]

Though it has been reported the transformed phase and exsolved nanoparticles work synergistically, the order of transformation and exsolution is still not clear. The phase transitions may occur earlier than the exsolution and act as a driving force to trigger the emergence of B-site metals.[30] The order of phase transitions and exsolution could be varied for the different material systems, for example, the exsolution of metallic particles prior to phase transition was observed in $La_{0.5}Sr_{0.5}Fe_{0.8}Ni_{0.1}Nb_{0.1}O_{3-\delta}$.[207]

5.2.2. *Self-assembly material together with metal nanoparticles*

Distinct from solely metal nanoparticle exsolution, other oxide particles may segregate together to form a special structure that boosts CO production. This situation was first reported on fluorite, rutile, spinel and other non-perovskite ceramic materials that experience a phase separation during the reduction, such as $Ce_{1-x}Ni_xO_2$,[149] $NiMnO_4$,[162] Ni and Cu doped $Nb_{1.33}Ti_{0.67}O_4$,[150] $NbTi_{0.5}Ni_{0.5}O_4$,[151] $Ni_{0.9}TiO_3$,[153] Ni–Cr_2O_3,[161] etc. The significantly created metal-oxide active interfaces may serve to promote CO_2 reduction and subsequently improve the performance of electrolyzer.[208] Metallic species generated from Fe, Ni and Co-doped $Sm_{0.1}Ce_{0.8}O_{2-\delta}$ under the reduction of CO.[192] Different from the isolated Fe nanoparticles, both Ni and Co species suffered with serve agglomeration. The CO_2 electrolysis cell with partially reduced Fe species on the cathode demonstrates a current density of 0.66 A cm^{-2} at 700 °C.

A reconstruction of the electrode during the operating conditions was reported for $Sr_2Fe_{1.5}Mo_{0.3}Cu_{0.2}O_{6-\delta}$.[195] The perovskite reconstructed into double perovskites, Ruddlesden-Popper and bimetallic phases, as shown in Fig. 11. The formed oxygen vacancy-rich together with metal phases together display high Faradaic efficiencies and current density (1.94 A cm^{-2} at 1.4 V). This observation allows one to regard the electronic properties of perovskites as originating exclusively from the BO_3 part of the ABO_3, particularly from the BO_6 octahedra. The reduction of Mo-doped $La_{0.55}Sr_{0.45}Fe_{0.85}Mo_{0.15}O_3$ can form Fe–Mo–O oxides, $(La,Sr)_2(Mo,Fe)O_4$ instead of the decomposition of SrO and $SrCO_3$ on the superficial of electrode for the undoped composition.[180] Similar phenomenon was reported in Ru doped $Pr_{0.4}Sr_{0.6}Fe_{0.9}Mo_{0.1}O_{3-\delta}$ material with a Fe–Ru alloy particles exsolved accompany the formation of Sr_2RuO_4. The current dentiy of the electrolyser was almost doubled (~1.48 A cm^{-2}) at 800 °C under 2.0 V. The formed metal-oxides heterostructures provide a job-sharing function.[209]

The same phenomenon was discovered in perovskites, such as CeO_2 in $La_{0.8}Ce_{0.1}$ $Ni_{0.4}Ti_{0.6}O_{3-\delta}$[210] and MnO_x in $(Pr,Ba)_2Mn_{2-y}Fe_yO_{5+\delta}$.[167] Besides the formation of simple oxides, the $Pr_{0.2}Ca_{0.8}Fe_{0.8}Ni_{0.2}O_{3-\delta}$ self-assembled into perovskite $Pr(Ca)Fe(Ni)O_{3-\delta}$ and brownmillerite $Ca_2Fe_2O_5$ dual-phase composite during the calcination.[211] Umit S. Ozkan et al. investigate the exsolution structure-electrocatalysis performance on La/$SrFeO_3$ system. The A-site excess leads to the formation of a carbonate layer, therefore, improving the performance.[212] The intensively designed segregation of alkaline earth oxides seems to provide adsorption and catalytic sites, thus improving the CO_2 electrolysis performance.[158] However, the formed carbonate seems to block the active site for the catalytic reaction, thus, there may be a trade-off between the carbonate layer and metal nanoparticles.[213] The stability of $La_{0.5}Sr_{0.5}Fe_{1-x}Co_xO_3$ under reduction atmosphere was improved by doping with high-valent niobium but resulting in limited CO_2 electrochemical reduction activities.[184]

5.2.3. *Electrochemical switching exsolution in the CO_2 electrolysis cell*

The electrochemical activation was applied as an effective approach to facilitate the CO_2 electroreduction of the cathode.[146] The electrochemical activation drives the exsolution within serval minutes and produces uniform nanoparticles on the electrode surface.[214] The electrochemical switching can be easily performed in the electrolysis mode and achieve significant performance, as shown in Fig. 12.[196,215] When deliberate activate the electrode under applied potential, the polarization resistance was reduced significantly, as shown in Fig. 12a.[196,216,217] At the meanwhile, metallic species emerged on the electrode surface. The identification of surface species was used to illustrate the CO_2 reduction process, especially the formation of oxy-carbon adsorbate and metallic

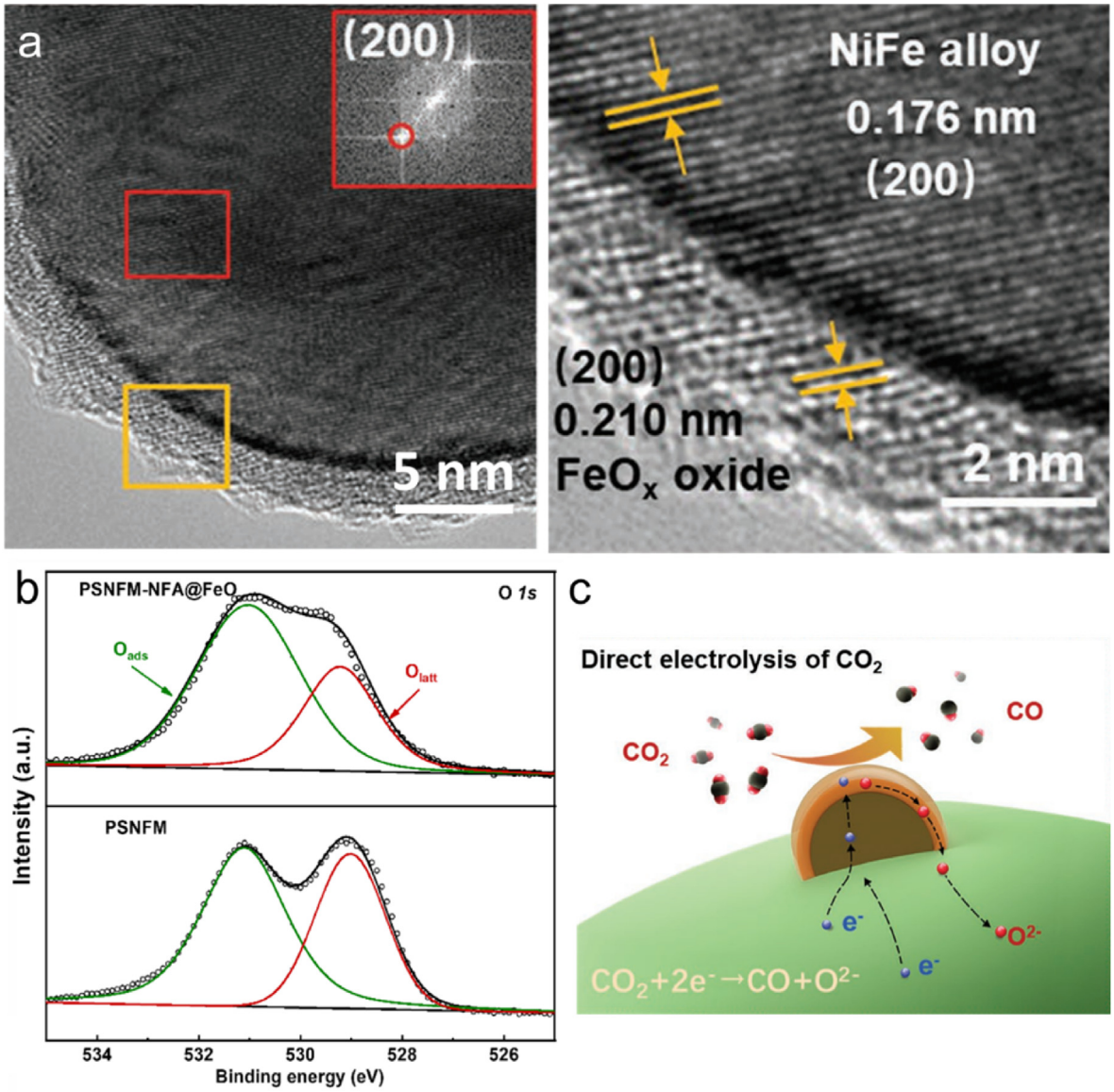

Fig. 9. NiFe particles exsolved on $Pr_{0.4}Sr_{1.6}(NiFe)_{1.5}Mo_{0.5}O_{6-\delta}$. (a) TEM images of NiFe particle with FeO shell. (b) XPS spectra of O 1s for samples before and after reduction. (c) Schematic illustration of CO_2 electrolysis process on cathode with core-shell alloy nanoparticle. Reproduced with permission from Ref. 186.

species. The contradictory results indicate the importance of studying the adsorption and desorption under the presence of nanoparticles.

Weishen Yang and Xuefeng Zhu et al. systematically studied the CO_2 electroreduction with $LaFeO_{3-\delta}$ (Ln = La, Pr and Gd) employed as cathodes.[218] The cathode undergoes surface reconstruction under applied voltage leading to the formation of oxygen vacancies and Fe nanoparticles. Though the switching exhibits a higher efficiency on the exsolution of nanoparticles, a sufficient potential and period are necessary to fully activate the electrode, especially under pure CO_2, as shown in Fig. 12b.[216] Similarly, a critical applied voltage seems needed to trigger the exsolution of Fe nanoparticles under electrochemical switching for a $Pr_{0.4}Sr_{0.6}Fe_{0.875}Mo_{0.125}O_{3-\delta}$ based CO_2 SOEC.[219] Compared with a larger amount of research on chemical reduction with gases, the number of works reported on electrochemical reduction is still rare. The electrochemical switching needs to be further investigated to better illustrate its mechanism.[220,221]

5.3. Reversibility of exsolution in the CO_2 electrolysis cell

The exsolution study was first proposed in catalyst field as a 'smart' catalyst, where the Pd exsolved from $LaFe_{0.57}Co_{0.38}Pd_{0.05}O_3$ possess reversibility during the redox process.[52] Non-perovskite materials provide well-matched thermal expansion coefficients with electrolyte. Spinel oxide $CaFe_2O_4$ undergoes a phase transition to produce exsolved Fe nanoparticles together with brownmillerites.[194] Moreover, the original structure can be recovered by calcining at higher temperature in air, as shown in Fig. 13a. This material therefore exhibits reversibility under the redox process under an electroreduction atmosphere. The exsolution of Co assists the emergence of Fe in generating CoFe alloy nanoparticles that oxidize into $CoFeO_x$ and then dissolve into the double perovskites under an oxidizing atmosphere.[172] This evolution was monitored with in-situ TEM under different conditions, as shown in Fig. 13b. The reversibility of CoFe renders the catalyst redox stability for about 12 cycles.

The exsolved nanoparticles were reversible during the redox cycles. The electrolysis performance was significantly improved with the synergy effect of exsolved nanoparticles. It was about 50% improvement for the cathode as catalytic active Ni nanoparticles facilitate ion conduction in titanate mixed with SDC and enhance the electrocatalytic activity for electrolysis of CO_2. This synergetic exsolution effect was also disclosed in

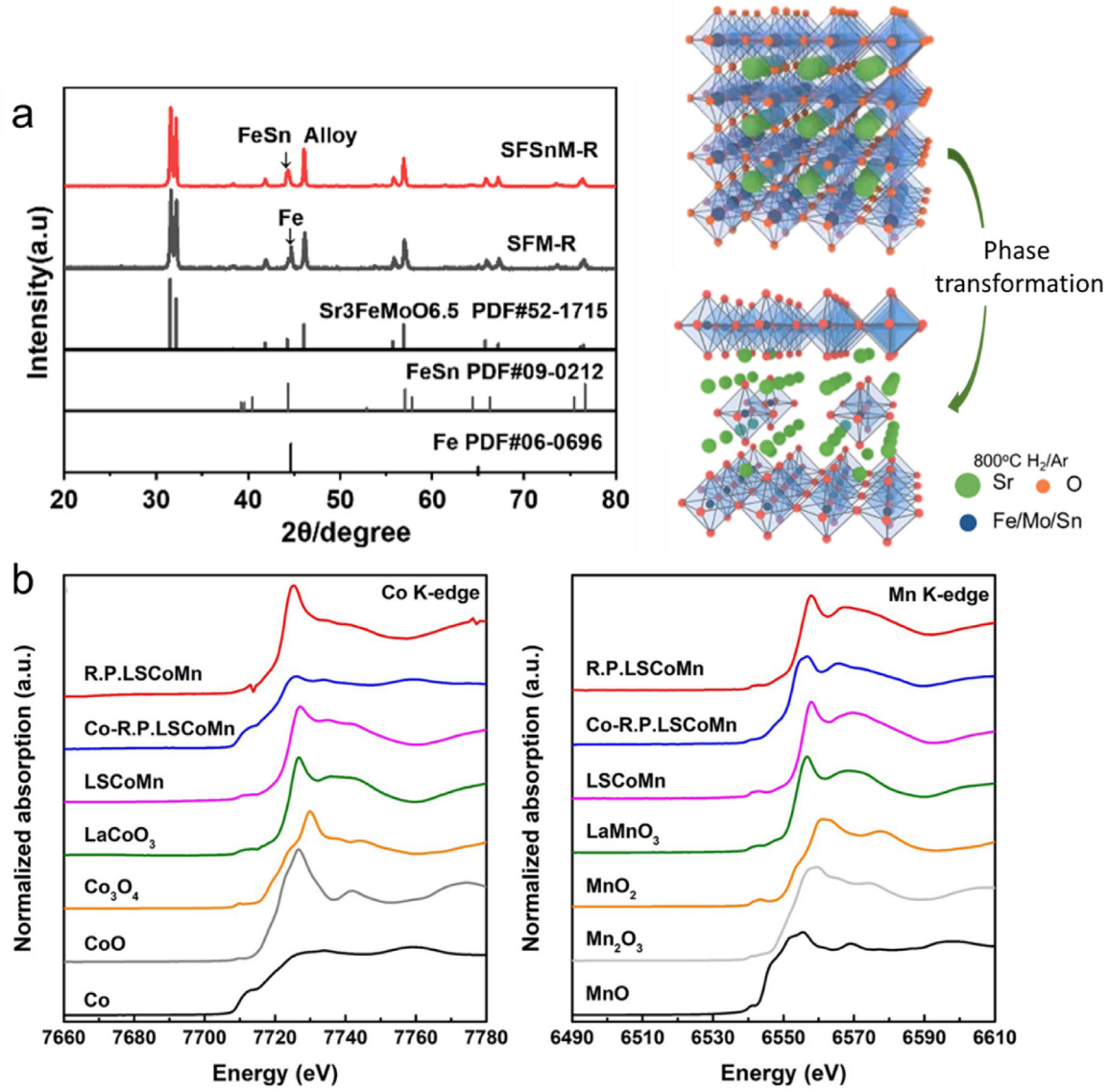

Fig. 10. Phase transformation materials in CO_2 electroreduction. (a) XRD pattern and schematic illustration of $Sr_{1.95}Fe_{1.4}Sn_{0.1}Mo_{0.5}O_{6-\delta}$ phase structure transformation under reduction. Reproduced with permission from Ref. 181. (b) XANES spectra of Co and Mn in $La_{0.6}Sr_{0.4}Co_{0.7}Mn_{0.3}O_3$ during the exsolution. Reproduced with permission from Ref. 89.

$(La_{0.65}Sr_{0.3}\ Ce_{0.05})_{0.9}(Cr_{0.5}Fe_{0.5})_{0.85}Ni_{0.15}O_{3-\delta}$ where the Ni doping reduces the segregation energy of Fe subsequent with the generation of NiFe alloy particles.[169]

5.4. Role of interface in the exsolved electrode

The metal-oxide interface generated by the exsolution of nanoparticles addresses a crucial role in promoting CO_2 adsorption and activation.[171] The abundant oxygen vacancies generated on the periphery of the socketed nanoparticles contribute to the improved activation of CO_2 on electrodes proofed by the distribution of relaxation time analysis combined with density functional theory calculations.[117] The DFT calculation results demonstrate that the bidentate configuration and carbonates formation for CO_2 chemisorption exhibit low energy scenarios.[18,179,196]

The sluggish diffusion process of dopant cations inside the bulk perovskite suppresses the generation of abundant metal/oxide interfaces. Interestingly, the repeated redox cycles provide an enriched dopant subsurface which promoted the exsolution population of RuFe nanoparticles on $Sr_2Fe_{1.4}Ru_{0.1}Mo_{0.5}O_{6-\delta}$ perovskite.[177] Metal-oxide interface formed at the border of nanoparticles can be seen in Fig. 14a, which facilitates the CO_2 adsorption at low temperature compared with either metal or oxide alone. High-temperature reduction treatment of $Sr_{1.9}Fe_{1.5}Mo_{0.4}Ni_{0.1}O_{6-\delta}$ can produce hetero-structure perovskite mixtures.[178] In the meanwhile, the exsolved FeCu bimetallic nanoparticles create a metal-oxide interface that makes the electrode even more active for CO_2 electrolysis with a current density of 2.5 A cm^{-2} at 1.5 V.

The emerged Ni nanoparticles and the doped multivalence species, such as Mn, Mo and Fe afford synergy effect to facilitate CO_2 reduction.[18,193] The oxygen exchange coefficient was enhanced with the formation of metal-oxide interface accompanied with exsolution from the electrical conductivity relaxation results, as shown in Fig. 14b. Based on therotical calculation, the CO_2 adsorbed across the interface between the exsolved metals (Ni, Cu and alloy) and titanate from $(La_{0.2}Sr_{0.8})_{0.9}Ti_{0.5}Mn_{0.4}Cu_{0.1}O_{3-\delta}$.[193] Kui Xie et al. explored the metal-oxide interface with nanoparticles decorated electrodes in the CO_2 electrolyzer with perovskites, including Cu[148] and Ni[154] doped $(La_{0.75}Sr_{0.25})_{0.9}Cr_{0.5}Mn_{0.5}O_{3-\delta}$,[154] $(La_{0.3}Sr_{0.7})_{0.9}Ti_{0.95}Ni_{0.05}O_{3-\delta}$,[152,156,170,193] $La_{0.75}Sr_{0.25}Cr_{0.5-x}Fe_{0.5}Ti_xO_{3-\delta}$,[222] Ni-doped $SrFeO_3$,[159] and

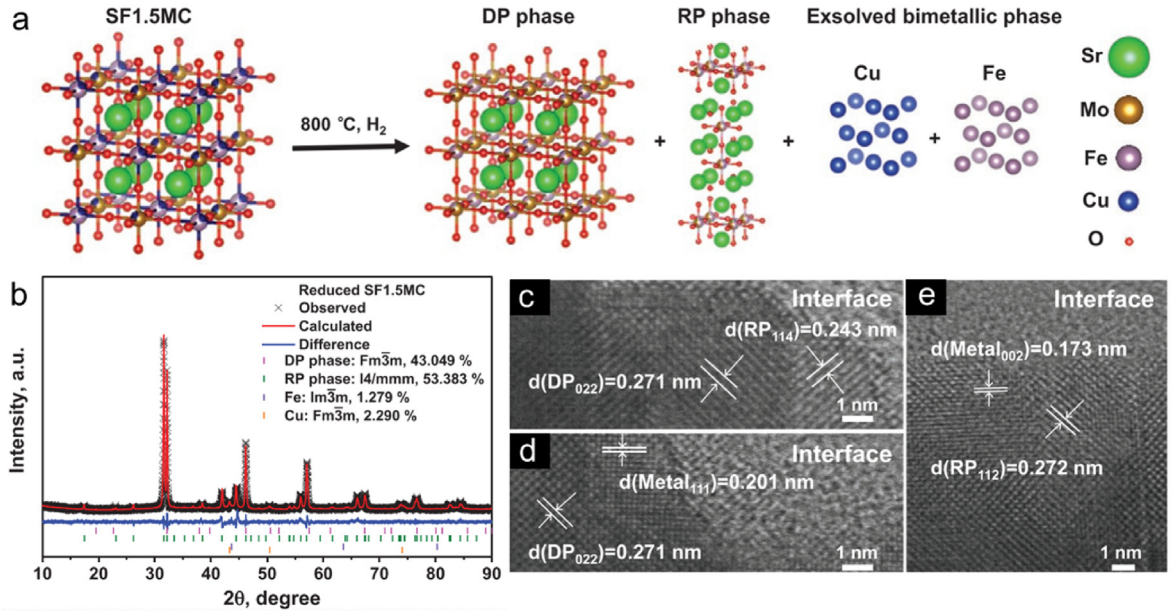

Fig. 11. Self-assembly with phase segregation into different phases under operation. (a) Schematics of the phase segregation of $Sr_2Fe_{1.5}Mo_{0.3}Cu_{0.2}O_{6-\delta}$. (b) XRD of the reduced samples. (c) HRTEM image of the double perovskites - Ruddlesden-Popper interface. (d) Double perovskites interface. (e) Ruddlesden-Popper interface. Reproduced with permission from Ref. 195.

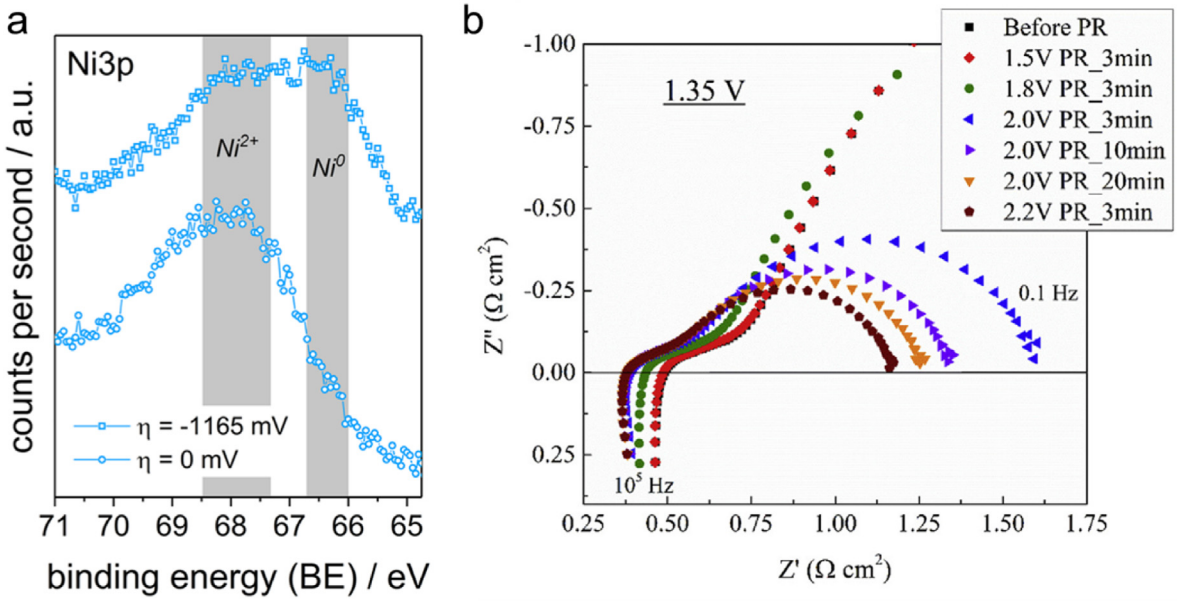

Fig. 12. Exsolution activated by electrochemical switching in the CO_2 electrolysis cell. (a) Ni 3p XPS spectra for $La_{0.8}Sr_{0.2}Cr_{0.9}Ni_{0.1}O_{3-\delta}$ with and without cathodic polarization showing the exsolution of Ni. Reproduced with permission from Ref. 217. (b) Impedance spectra of $La_{0.43}Ca_{0.37}Ni_{0.06}Ti_{0.94}O_3$ perovskite cell under electrochemical switching in CO_2. Reproduced with permission from Ref. 215.

$Sr_2Fe_{1.5+x}Mo_{0.5}O_{6-\delta}$.[223] The CO productivity and Faraday efficiency was improved by forming nanoparticles as the metal-oxide interface length increased with the exsolved particle amount, as shown in Fig. 14c.

Ceria as a prototype oxide has been widely studied to understand the functions of oxygen vacancy in various applications.[224,225] To increase the oxygen vacancy concentration on the electrode, the infiltration combined with exsolution was used to fabricate the CO_2 electrolysis cell.[188] The CeO_{2-x} formed on the electrode surface boosts the number of oxygen vacancies and contributes to decreased polarization resistance. The ceria-metal/titanate heterostructure was constructed by a co-exsolving method with devised post-treatments.[210] Contributing to the presence of ceria, the availability of electrons and ion was significantly improved, resulting in enhanced electrochemical activities of electrodes.

6. Challenges and perspectives

To meet the demands of the market, a CO_2 SOEC system based on multifunctional oxide is essential as a complement to the traditional materials that have been successfully utilized in space exploration.[226,227] Exsolved materials are potential candidates for achieving this objective. Nevertheless, further exploitations, such as the development of high ionic

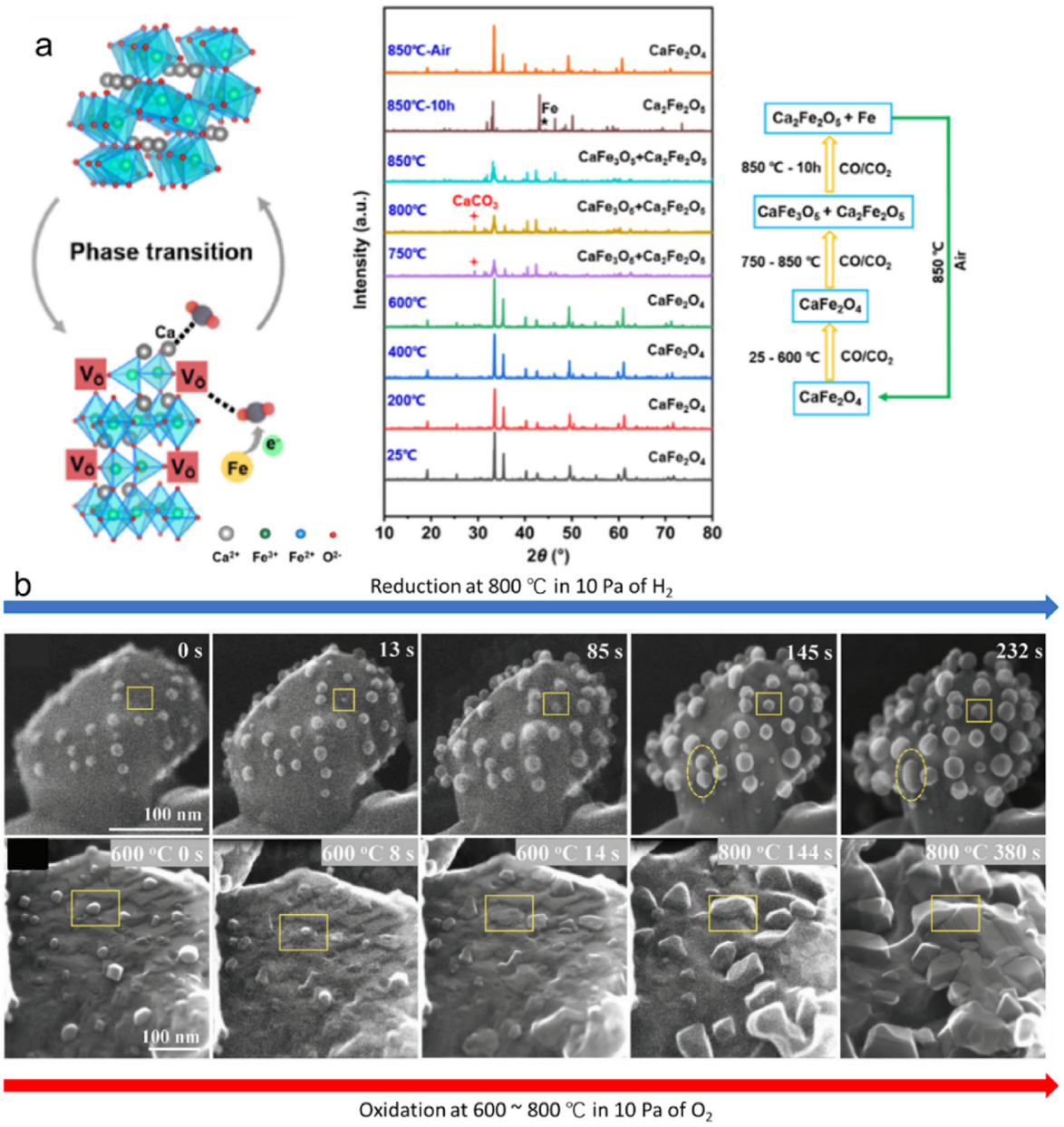

Fig. 13. Reversibility of exsolved materials in CO_2 electroreduction. (a) Schematic illustration of reversibility for $CaFe_2O_4$ under the 80% CO/20% CO_2 atmosphere and re-oxidized in air and in-situ XRD of different temperature. Reproduced with permission from Ref. 194. In-situ STEM images of $Sr_2Fe_{1.35}Mo_{0.45}Co_{0.2}O_{6-\delta}$ in reduction and re-oxidation. Reproduced with permission from Ref. 172.

conductivity, model systems, in-situ characterization techniques, modeling and calculation, are necessary to obtain a better understanding of the intrinsic properties of the exsolution. Without these advancements, our understanding of exsolution phenomena remains limited.

(1) New exsolution materials and driven forces

Although the metal-oxide interface produced by the emergence of nanoparticles promotes the electrolysis performance, the ionic conductivity still seems limited, especially for the single composition system.[176,228,229] Therefore, the development of novel materials with both high catalytic activity and ionic conductivity is crucial for building highly efficient CO_2 electrolyzers. To achieve this, it is necessary to selectively drive cations out from the material while maintaining stability and activity. Additionally, controlling nucleation on the surface, rather than in bulk, is of greater significance for increasing the atomic efficiency of exsolved materials.

(2) In-situ techniques

Understanding the degradation of electrodes at higher potential/current density will be the key to prolonging the lifetime of high-temperature CO_2 electrolyzers. However, ex-situ measurements are not sufficient to detect metastable adsorbates that only form under operating conditions.[217] To better understand the rate-determined factors related to both surface chemistry and electrochemical reactions, in-situ or operando characterization techniques, such as ambient-pressure XPS,[230,231] in-situ XAS, environment-TEM and high-temperature Raman, are necessary. These techniques are crucial for uncovering surface reconstruction and interface evolution, which may play a vital role

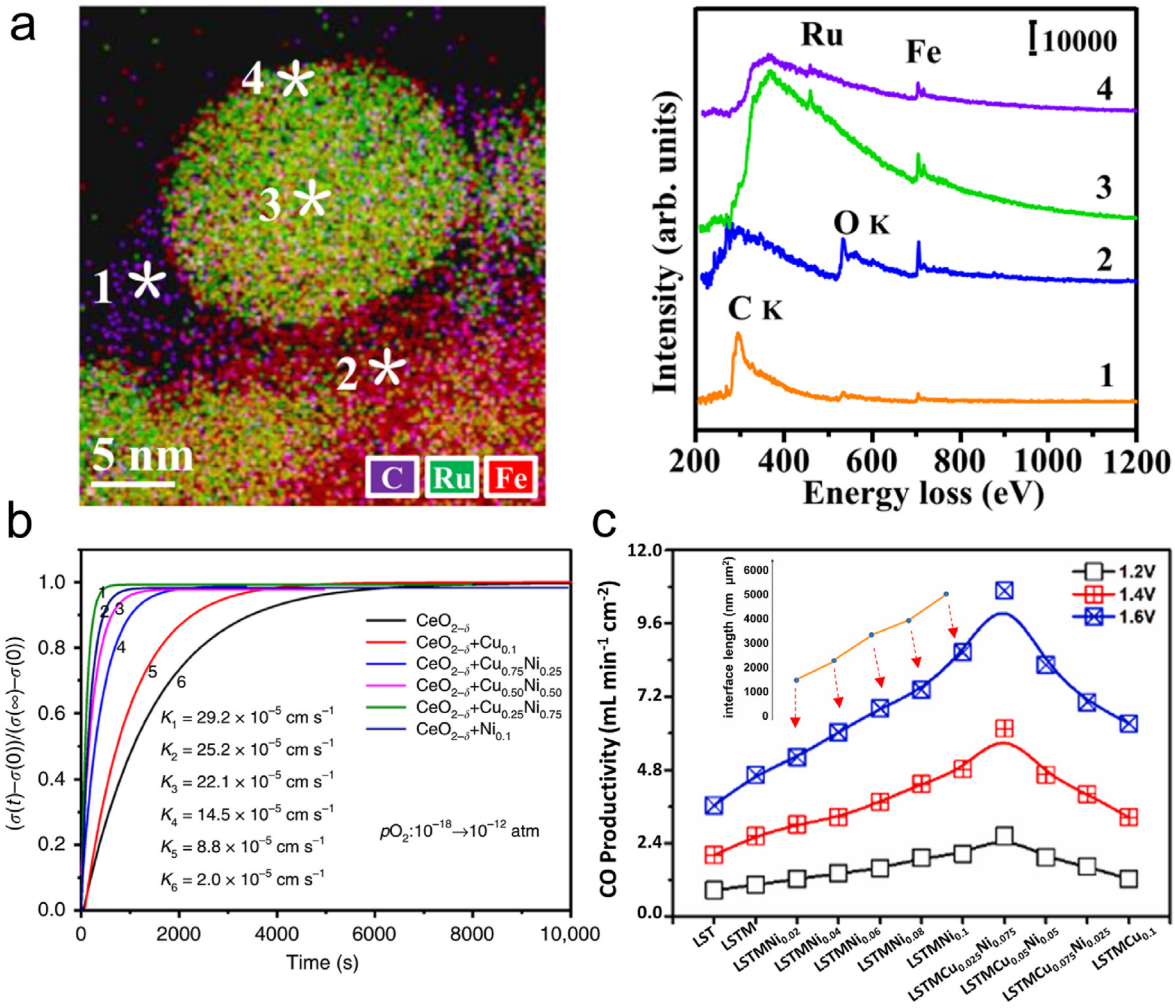

Fig. 14. Role of metal-oxide interface in CO_2 SOECs. (a) STEM-EDX map and EELS spectra for Ru nanoparticle exsolved from $Sr_2Fe_{1.4}Ru_{0.1}Mo_{0.5}O_{6-\delta}$. Reproduced with permission from Ref. 177. (b) Oxygen transfer at interfaces tested using electrical conductivity relaxation. Reproduced with permission from Ref. 162. (c) CO productivity and Faraday efficiency with different cathodes in SOEC test at 800 °C. Different interface length as inset. Reproduced with permission from Ref. 193.

in enhancing the performance of electrocatalytic reactions.

(3) Model system

The non-uniform porosity and structural defects in powder material can either promote or hinder the exsolution, making research into the phenomenon more complex. To uncover the underlying mechanism for the driving force and exsolution, well-defined geometry model systems are needed, such as determining the quantitative relationship between oxygen deficiency, electrochemical switching potential, and exsolved nanoparticles. To aid in this effort, the thin film systems combined with in-situ techniques, such as Electrochemical impedance spectroscopy (EIS),[232] surface-sensitive XRD[44] and APXPS,[233] can elucidate more insights into the exsolution process.

(4) Machine learning and calculation

The application of artificial intelligence techniques is revolutionizing research. Advanced computational tools, such as high-throughput screening on neural network[234] and mechine-learning,[235] are becoming increasingly important in the design of novel materials and understanding of the evolution process. The machine learning provides an efficient way to simplify the indispensable complex high-throughput simulation and calculations. The machine learning approach is crucial for screening huge potential materials with suitable descriptor, such as the oxygen p-band centre, the vacancy formation energy, the charge-transfer energy and the Lewis acid strength. Thus, a key for developing high-efficient machine learning method is obtaining an universal descripter which requires well-understanding of the mechanism of reactions.[236] Besides, the this approach can be used to optimized a specific material system where a descripter was widely accepted.[237]

To conclude, the exsolved materials show great potential in high-temperature CO_2 reduction cells. Further research should be done to explore their full application, both in terms of fundamental understanding and engineering implementation. Opportunities for using exsolved materials in the future remain largely unexplored, and their full potential must be explored.

Declaration of competing interest

The authors declare that they have no known competing financial interests or personal relationships that could have appeared to influence the work reported in this paper.

Acknowledgments

This work is supported by the National Key Research and Development Program of China (No. 2021YFA0718900) and the National Natural Science Foundation of China (No. NSCF52102137). We also appreciate the support from Tsinghua University Initiative Scientific Research

Program and Open Funds of the State Key Laboratory of Rare Earth Resource Utilization (RERU2022006EPSRC) and the Institute for Guo Qiang, Tsinghua University (2020GQG1003).

References

1. CO_2, D. https://www.co2.earth/global-co2-emissions.
2. Spinner NS, Vega JA, Mustain WE. Recent progress in the electrochemical conversion and utilization of CO_2. *Catal Sci Technol*. 2012;2(1):19–28.
3. Sovacool BK, Griffiths S. Culture and low-carbon energy transitions. *Nat Sustain*. 2020;3(9):685–693.
4. Weissbart JSWH, Inami SH, McCullough CM, Ring SA. *Development of a CO_2-H_2O solid oxide electrolyte electrolysis system; National Aeronautics and Space Administration Ames Research Center: Moffett Field, California*. 1969.
5. Zheng Y, Wang J, Yu B, et al. A review of high temperature co-electrolysis of H_2O and CO_2 to produce sustainable fuels using solid oxide electrolysis cells (SOECs): advanced materials and technology. *Chem Soc Rev*. 2017;46(5):1427–1463.
6. Graves C, Ebbesen SD, Mogensen M, Lackner KS. Sustainable hydrocarbon fuels by recycling CO_2 and H_2O with renewable or nuclear energy. *Renew Sustain Energy Rev*. 2011;15(1):1–23.
7. Hauch A, Kungas R, Blennow P, et al. Recent advances in solid oxide cell technology for electrolysis. *Science*. 2020;370(6513), eaba6118.
8. Barbi GB, Mari CM. High temperature water electrolysis: the cathodic process at the cermet (Pt+$La_{0.8}Sr_{0.2}CrO_3$)/Zirconia interface. *Solid State Ionics*. 1988;26(3):243–250.
9. Ishihara T, Jirathiwathanakul N, Zhong H. Intermediate temperature solid oxide electrolysis cell using $LaGaO_3$ based perovskite electrolyte. *Energy Environ Sci*. 2010;3(5):665–672.
10. Sune Dalgaard Ebbesen. X. S. a. M. B. M., Understanding the processes governing performance and durability of solid oxide electrolysis cells. *Faraday Discuss*. 2015;182:393–422.
11. Chen K, Jiang SP. Review—materials degradation of solid oxide electrolysis cells. *J Solid State Electrochem*. 2016;163(11):F3070–F3083.
12. Graves C, Ebbesen SD, Mogensen M. Co-electrolysis of CO_2 and H_2O in solid oxide cells: performance and durability. *Solid State Ionics*. 2011;192(1):398–403.
13. Yue X, Irvine JTS. Alternative cathode material for CO_2 reduction by high temperature solid oxide electrolysis cells. *J Electrochem Soc*. 2012;159(8):F442–F448.
14. Song Y, Zhou Z, Zhang X, et al. Pure CO_2 electrolysis over an Ni/YSZ cathode in a solid oxide electrolysis cell. *J Mater Chem*. 2018;6(28):13661–13667.
15. Ye L, Xie K. High-temperature electrocatalysis and key materials in solid oxide electrolysis cells. *J Energy Chem*. 2021;54:736–745.
16. Jiang Y, Chen F, Xia C. A review on cathode processes and materials for electro-reduction of carbon dioxide in solid oxide electrolysis cells. *J Power Sources*. 2021;493:229713.
17. Ni C, Zhou J, Zhang Z, et al. Iron-based electrode materials for solid oxide fuel cells and electrolysers. *Energy Environ Sci*. 2021;14(12):6287–6319.
18. Ye L, Zhang M, Huang P, et al. Enhancing CO_2 electrolysis through synergistic control of non-stoichiometry and doping to tune cathode surface structures. *Nat Commun*. 2017;8:14785.
19. Rosen BA. Progress and opportunities for exsolution in electrochemistry. *Electrochem*. 2020;1(1):32–43.
20. Sun X, Chen H, Yin Y, et al. Progress of exsolved metal nanoparticles on oxides as high performance (electro)catalysts for the conversion of small molecules. *Small*. 2021;17(10):2005383.
21. Tezel E, Whitten A, Yarema G, Denecke R, McEwen J-S, Nikolla E. Electrochemical reduction of CO_2 using solid oxide electrolysis cells: insights into catalysis by nonstoichiometric mixed metal oxides. *ACS Catal*. 2022;12(18):11456–11471.
22. Irvine JTS, Neagu D, Verbraeken MC, Chatzichristodoulou C, Graves C, Mogensen MB. Evolution of the electrochemical interface in high-temperature fuel cells and electrolysers. *Nat Energy*. 2016;1(1):15014.
23. Neagu D, Tsekouras G, Miller DN, Menard H, Irvine JTS. In situ growth of nanoparticles through control of non-stoichiometry. *Nat Chem*. 2013;5(11):916–923.
24. Li B, Katz MB, Duan Y, et al. Joint theoretical and experimental study of phase equilibria and evolution in Pt-doped calcium titanate under redox conditions. *Chem Mater*. 2014;27(1):18–28.
25. Lee Y-L, Kleis J, Rossmeisl J, Morgan D. Ab initio energetics of $LaBO_3$(001)(B=Mn, Fe, Co, and Ni) for solid oxide fuel cell cathodes. *Phys Rev B*. 2009;80(22):224101–224120.
26. Hamada I, Uozumi A, Morikawa Y, Yanase A, Katayama-Yoshida H. A density functional theory study of self-regenerating catalysts $LaFe_{1-x}M_xO_{3-y}$ (M = Pd, Rh, Pt). *J Am Chem Soc*. 2011;133(46):18506–18509.
27. Gao Y, Lu Z, You TL, et al. Energetics of nanoparticle exsolution from perovskite oxides. *J Phys Chem Lett*. 2018;9(13):3772–3778.
28. Gao Y, Xing C, Hu S, Zhang S. In situ exsolved Au nanoparticles from perovskite oxide for efficient epoxidation of styrene. *J Mater Chem*. 2021;9(16):10374–10384.
29. Kwon O, Sengodan S, Kim K, et al. Exsolution trends and co-segregation aspects of self-grown catalyst nanoparticles in perovskites. *Nat Commun*. 2017;8:15967.
30. Sun YF, Zhang YQ, Chen J, et al. New opportunity for in Situ exsolution of metallic nanoparticles on perovskite parent. *Nano Lett*. 2016;16(8):5303–5309.
31. Kwon H, Lee W, Han JW. Suppressing cation segregation on lanthanum-based perovskite oxides to enhance the stability of solid oxide fuel cell cathodes. *RSC Adv*. 2016;6(74):69782–69789.
32. Mebane DS. A variational approach to surface cation segregation in mixed conducting perovskites. *Comput Mater Sci*. 2015;103:231–236.
33. Christian JW. *The Theory of Transformations in Metals and Alloys*. Elsevier; 2002.
34. Wang Z, Cheng Y, Shao X, et al. Ping Jiang, S.; Parkinson, G.; Buckley, C.; Li, C.-Z., Nanocatalysts anchored on nanofiber support for high syngas production via methane partial oxidation. *Appl Catal, A*. 2018;565:119–126.
35. An Y-T, Choi B-H, Ji M-J, Lee K-J, Hwang HJ. New fabrication technique for a Ni–YSZ composite anode from a core–shell structured particle. *Solid State Ionics*. 2012;207:64–68.
36. Yanagisawa S, Uozumi A, Hamada I, Morikawa Y. Search for a self-regenerating perovskite catalyst using ab initio thermodynamics calculations. *J Phys Chem C*. 2013;117(3):1278–1286.
37. Kizaki H, Kusakabe K, Nogami S, Katayama-Yoshida H. Generation of nano-catalyst particles by spinodal nano-decomposition in perovskite. *APEX*. 2008;1:104001–104003.
38. Gao Y, Chen D, Saccoccio M, Lu Z, Ciucci F. From material design to mechanism study: nanoscale Ni exsolution on a highly active A-site deficient anode material for solid oxide fuel cells. *Nano Energy*. 2016;27:499–508.
39. Kim KJ, Han H, Defferriere T, et al. Facet-dependent in situ growth of nanoparticles in epitaxial thin films: the role of interfacial energy. *J Am Chem Soc*. 2019;141(18):7509–7517.
40. Tan J, Lee D, Ahn J, Kim B, Kim J, Moon J. Thermally driven in situ exsolution of Ni nanoparticles from (Ni, Gd)CeO_2 for high-performance solid oxide fuel cells. *J Mater Chem*. 2018;6(37):18133–18142.
41. Pilger F, Testino A, Carino A, et al. Size control of Pt clusters on CeO_2 nanoparticles via an incorporation–segregation mechanism and study of segregation kinetics. *ACS Catal*. 2016;6(6):3688–3699.
42. Kwon O, Joo S, Choi S, Sengodan S, Kim G. Review on exsolution and its driving forces in perovskites. *J. Phys. Energy*. 2020;2, 032001.
43. Opitz AK, Nenning A, Rameshan C, et al. Enhancing electrochemical water-splitting kinetics by polarization-driven formation of near-surface iron(0): an in situ XPS study on perovskite-type electrodes. *Angew Chem Int Ed*. 2015;54(9):2628–2632.
44. Opitz AK, Nenning A, Vonk V, et al. Understanding electrochemical switchability of perovskite-type exsolution catalysts. *Nat Commun*. 2020;11(1):4801.
45. Sun YF, Yang YL, Chen J, et al. Toward a rational photocatalyst design: a new formation strategy of co-catalyst/semiconductor heterostructures via in situ exsolution. *Chem. Commun*. 2018;54(12):1505–1508.
46. Kyriakou V, Sharma RK, Neagu D, et al. Plasma driven exsolution for nanoscale functionalization of perovskite oxides. *Small Methods*. 2021;12(5), 2100868.
47. Khalid H, Haq Au, Alessi B, et al. Rapid plasma exsolution from an A-site deficient perovskite oxide at room temperature. *Adv Energy Mater*. 2022, 2201131.
48. Sun Y, Li J, Zeng Y, et al. A-site deficient perovskite: the parent for in situ exsolution of highly active, regenerable nano-particles as SOFC anodes. *J Mater Chem*. 2015;3(20):11048–11056.
49. Yu N, Jiang G, Liu T, et al. Understanding the A-site non-stoichiometry in perovskites: promotion of exsolution of metallic nanoparticles and the hydrogen oxidation reaction in solid oxide fuel cells. *Sustain Energy Fuels*. 2021;5(2):401–411.
50. Han H, Park J, Nam SY, et al. Lattice strain-enhanced exsolution of nanoparticles in thin films. *Nat Commun*. 2019;10(1):1471.
51. Tsvetkov N, Lu Q, Sun L, Crumlin EJ, Yildiz B. Improved chemical and electrochemical stability of perovskite oxides with less reducible cations at the surface. *Nat Mater*. 2016;15(9):1010–1016.
52. Nishihata Y, Mizuki J, Akao T, et al. Self-regeneration of a Pd-perovskite catalyst for automotive emissions control. *Nature*. 2002;418(6894):162–164.
53. Zhu Y, Zhou W, Ran R, Chen Y, Shao Z, Liu M. Promotion of oxygen reduction by exsolved silver nanoparticles on a perovskite scaffold for low-temperature solid oxide fuel cells. *Nano Lett*. 2016;16(1):512–518.
54. Zhang Y-Q, Tao H-B, Liu J, et al. A rational design for enhanced oxygen reduction: strongly coupled silver nanoparticles and engineered perovskite nanofibers. *Nano Energy*. 2017;38:392–400.
55. Kothari M, Jeon Y, Miller DN, et al. Platinum incorporation into titanate perovskites to deliver emergent active and stable platinum nanoparticles. *Nat Chem*. 2021;13:677–682.
56. Tanaka H, Taniguchi M, Uenishi M, et al. Self-regenerating Rh- and Pt-based perovskite catalysts for automotive-emissions control. *Angew Chem Int Ed*. 2006;45(36):5998–6002.
57. Glaser R, Zhu T, Troiani H, Caneiro A, Mogni L, Barnett S. The enhanced electrochemical response of $Sr(Ti_{0.3}Fe_{0.7}Ru_{0.07})O_{3-\delta}$ anodes due to exsolved Ru–Fe nanoparticles. *J Mater Chem*. 2018;6(12):5193–5201.
58. Kim GS, Lee BY, Ham HC, et al. Highly active and stable $Sr_{0.92}Y_{0.08}Ti_{1-x}Ru_xO_{3-d}$ in dry reforming for hydrogen production. *Int J Hydrogen Energy*. 2019;44(1):202–212.
59. Jang JS, Kim JK, Kim K, et al. Dopant-driven positive reinforcement in Ex-solution process: new strategy to develop highly capable and durable catalytic materials. *Adv Mater*. 2020;32(46), e2003983.
60. Dai S, Zhang S, Katz MB, Graham GW, Pan X. In situ observation of Rh-$CaTiO_3$ catalysts during reduction and oxidation treatments by transmission electron microscopy. *ACS Catal*. 2017;7(3):1579–1582.
61. Jo YR, Koo B, Seo MJ, et al. Growth kinetics of individual Co particles ex-solved on $SrTi_{0.75}Co_{0.25}O_{3-\delta}$ polycrystalline perovskite thin films. *J Am Chem Soc*. 2019;141(16):6690–6697.
62. Adijanto L, Balaji Padmanabhan V, Küngas R, Gorte RJ, Vohs JM. Transition metal-doped rare earth vanadates: a regenerable catalytic material for SOFC anodes. *J Mater Chem*. 2012;22(22):11396–11402.

63. Thalinger R, Gocyla M, Heggen M, Klotzer B, Penner S. Exsolution of Fe and SrO nanorods and nanoparticles from lanthanum strontium ferrite $La_{0.6}Sr_{0.4}FeO_{3-\delta}$ materials by hydrogen reduction. *J Phys Chem C*. 2015;119(38):22050–22056.
64. Tang C, Kousi K, Neagu D, Metcalfe IS. Trends and prospects of bimetallic exsolution. *Chem Eur J*. 2021;27(22):6666–6675.
65. Neagu D, Oh TS, Miller DN, et al. Nano-socketed nickel particles with enhanced coking resistance grown in situ by redox exsolution. *Nat Commun*. 2015;6(1):8120.
66. Zhang L, Yang C, Frenkel AI, et al. Co-generation of electricity and chemicals from propane fuel in solid oxide fuel cells with anode containing nano-bimetallic catalyst. *J Power Sources*. 2014;262:421–428.
67. Liu S, Chuang KT, Luo J-L. Double-layered perovskite anode with in situ exsolution of a Co–Fe alloy to cogenerate ethylene and electricity in a proton-conducting ethane fuel cell. *ACS Catal*. 2015;6(2):760–768.
68. Liu S, Liu Q, Luo J-L. Highly stable and efficient catalyst with in Situ exsolved Fe–Ni alloy nanospheres socketed on an oxygen deficient perovskite for direct CO_2 electrolysis. *ACS Catal*. 2016;6(9):6219–6228.
69. Li Y, Hu B, Xia C, Xu WQ, Lemmon JP, Chen F. A novel fuel electrode enabling direct CO_2 electrolysis with excellent and stable cell performance. *J Mater Chem*. 2017;5(39):20833–20842.
70. Chookajorn T, Murdoch HA, Schuh CA. Design of stable nanocrystalline alloys. *Science*. 2012;337(6097):951–954.
71. Kang B, Matsuda J, Ishihara T. Cu–Fe–Ni nano alloy particles obtained by exsolution from $Cu(Ni)Fe_2O_4$ as active anode for SOFCs. *J Mater Chem*. 2019;7(45):26105–26115.
72. Santaya M, Troiani HE, Caneiro A, Mogni LV. Ternary Ni–Co–Fe exsolved nanoparticles/perovskite system for energy applications: nanostructure characterization and electrochemical activity. *ACS Appl Energy Mater*. 2020;3(10):9528–9533.
73. Joo S, Kim K, Kwon O, et al. Enhancing thermocatalytic activities via up-shift of the d-band center of exsolved Co-Ni-Fe ternary alloy nanoparticles for dry reforming of methane. *Angew Chem Int Ed*. 2021;60:15912–15919.
74. Périllat-Merceroz C, Gauthier G, Roussel P, Huvé M, Gélin P, Vannier R-N. Synthesis and study of a Ce-doped La/Sr titanate for solid oxide fuel cell anode operating directly on methane. *Chem Mater*. 2011;23(6):1539–1550.
75. Li M, Pietrowski MJ, De Souza RA, et al. A family of oxide ion conductors based on the ferroelectric perovskite $Na_{0.5}Bi_{0.5}TiO_3$. *Nat Mater*. 2014;13(1):31–35.
76. Zhang Y-Q, Tao H-B, Chen Z, et al. In situ grown cobalt phosphide (CoP) on perovskite nanofibers as an optimized trifunctional electrocatalyst for Zn–air batteries and overall water splitting. *J Mater Chem*. 2019;7(46):26607–26617.
77. Zhu Y, Dai J, Zhou W, Zhong Y, Wang H, Shao Z. Synergistically enhanced hydrogen evolution electrocatalysis by in situ exsolution of metallic nanoparticles on perovskites. *J Mater Chem*. 2018;6(28):13582–13587.
78. Kousi K, Tang C, Metcalfe IS, Neagu D. Emergence and future of exsolved materials. *Small*. 2021, e2006479.
79. Weber ML, Wilhelm M, Jin L, et al. Exsolution of embedded nanoparticles in defect engineered perovskite layers. *ACS Nano*. 2021;15(3):4546–4560.
80. Kosaka F, Noda N, Nakamura T, Otomo J. In situ formation of Ru nanoparticles on $La_{1-x}Sr_xTiO_3$-based mixed conducting electrodes and their application in electrochemical synthesis of ammonia using a proton-conducting solid electrolyte. *J Mater Sci*. 2016;52(5):2825–2835.
81. Lai K-Y, Manthiram A. Evolution of exsolved nanoparticles on a perovskite oxide surface during a redox process. *Chem Mater*. 2018;30(8):2838–2847.
82. Sun YF, Li JH, Cui L, et al. A-site-deficiency facilitated in situ growth of bimetallic Ni-Fe nano-alloys: a novel coking-tolerant fuel cell anode catalyst. *Nanoscale*. 2015;7(25):11173–11181.
83. Papargyriou D, Miller DN, Irvine JTS. Exsolution of Fe–Ni alloy nanoparticles from $(La,Sr)(Cr,Fe,Ni)O_3$ perovskites as potential oxygen transport membrane catalysts for methane reforming. *J Mater Chem*. 2019;7(26):15812–15822.
84. Chen X, Ni W, Wang J, Zhong Q, Han M, Zhu T. Exploration of Co-Fe alloy precipitation and electrochemical behavior hysteresis using lanthanum and cobalt co-substituted $SrFeO_{3-\delta}$ SOFC anode. *Electrochim Acta*. 2018;277:226–234.
85. Li J, Yu Y, Yin Y-M, Zhou N, Ma Z-F. A novel high performance composite anode with in situ growth of Fe-Ni alloy nanoparticles for intermediate solid oxide fuel cells. *Electrochim Acta*. 2017;235:317–322.
86. Managutti PB, Tymen S, Liu X, et al. Exsolution of Ni nanoparticles from A-site-deficient layered double perovskites for dry reforming of methane and as an anode material for a solid oxide fuel cell. *ACS Appl Mater Interfaces*. 2021;13(30):35719–35728.
87. Yang C, Li J, Lin Y, Liu J, Chen F, Liu M. In situ fabrication of CoFe alloy nanoparticles structured $(Pr_{0.4}Sr_{0.6})_3(Fe_{0.85}Nb_{0.15})_2O_7$ ceramic anode for direct hydrocarbon solid oxide fuel cells. *Nano Energy*. 2015;11:704–710.
88. Zhou J, Shin T-H, Ni C, et al. In situ growth of nanoparticles in layered perovskite $La_{0.8}Sr_{1.2}Fe_{0.9}Co_{0.1}O_{4-\delta}$ as an active and stable electrode for symmetrical solid oxide fuel cells. *Chem Mater*. 2016;28(9):2981–2993.
89. Park S, Kim Y, Han H, et al. In situ exsolved Co nanoparticles on Ruddlesden-Popper material as highly active catalyst for CO_2 electrolysis to CO. *Appl Catal B Environ*. 2019;248:147–156.
90. Pussacq T, Mentré O, Tessier F, et al. Nanometric nickel exsolution in the hexagonal perovskite $Ba_8Ta_6NiO_{24}$: survey of the structural, magnetic and catalytic features. *J Alloys Compd*. 2018;766:987–993.
91. Kwak NW, Jeong SJ, Seo HG, et al. In situ synthesis of supported metal nanocatalysts through heterogeneous doping. *Nat Commun*. 2018;9(1):4829.
92. Park YS, Kang M, Byeon P, et al. Fabrication of a regenerable Ni supported NiO-MgO catalyst for methane steam reforming by exsolution. *J Power Sources*. 2018;397:318–324.
93. Padi SP, Shelly L, Komarala EP, Schweke D, Hayun S, Rosen BA. Coke-free methane dry reforming over nano-sized $NiO-CeO_2$ solid solution after exsolution. *Catal Commun*. 2020;138:105951.
94. le Saché E, Pastor-Pérez L, Watson D, Sepúlveda-Escribano A, Reina TR. Ni stabilised on inorganic complex structures: superior catalysts for chemical CO_2 recycling via dry reforming of methane. *Appl Catal B Environ*. 2018;236:458–465.
95. Naeem MA, Abdala PM, Armutlulu A, Kim SM, Fedorov A, Müller CR. Exsolution of metallic Ru nanoparticles from defective, fluorite-type solid solutions $Sm_2Ru_xCe_{2-x}O_7$ to impart stability on dry reforming catalysts. *ACS Catal*. 2019;10(3):1923–1937.
96. Liu T, Zhao Y, Zhang X, et al. Robust redox-reversible perovskite type steam electrolyser electrode decorated with in situ exsolved metallic nanoparticles. *J Mater Chem*. 2020;8(2):582–591.
97. Neagu D, Papaioannou EI, Ramli WKW, et al. Demonstration of chemistry at a point through restructuring and catalytic activation at anchored nanoparticles. *Nat Commun*. 2017;8(1):1855.
98. Wang J, Yang J, Opitz AK, et al. Tuning point defects by elastic strain modulates nanoparticle exsolution on perovskite oxides. *Chem Mater*. 2021;33(13):5021–5034.
99. Agüero FN, Beltrán AM, Fernández MA, Cadús LE. Surface nickel particles generated by exsolution from a perovskite structure. *J Solid State Chem*. 2019;273:75–80.
100. Fang F, Feng N, Zhao P, et al. In situ exsolution of Co/CoO_x core-shell nanoparticles on double perovskite porous nanotubular webs: a synergistically active catalyst for soot efficient oxidation. *Chem Eng J*. 2019;372:752–764.
101. Zhou J, Yang J, Zong Z, et al. A mesoporous catalytic fiber architecture decorated by exsolved nanoparticles for reversible solid oxide cells. *J Power Sources*. 2020;468:228349–228359.
102. DeWulf DW, Jin T, Bard AJ. Electrochemical and surface studies of carbon dioxide reduction to methane and ethylene at copper electrodes in aqueous solutions. *J Electrochem Soc*. 1989;136(6):1686–1691.
103. Wang C, Li C, Liu J, Guo C. Engineering transition metal-based nanomaterials for high-performance electrocatalysis. *Mater. Rep.: Energy*. 2021;1(1):100006.
104. O'hayre R, Cha SW, Colella W, Prinz FB. John wiley & sons. *Fuel cell fundamentals*. 2016.
105. Neagu D, Irvine JTS. Structure and properties of $La_{0.4}Sr_{0.4}TiO_3$ ceramics for use as anode materials in solid oxide fuel cells. *Chem Mater*. 2010;22(17):5042–5053.
106. Zhang Y, Knibbe R, Sunarso J, et al. Recent progress on advanced materials for solid-oxide fuel cells operating below 500 °C. *Adv Mater*. 2017;29(48):1700132.
107. Connor PA, Yue X, Savaniu CD, et al. Tailoring SOFC electrode microstructures for improved performance. *Adv Energy Mater*. 2018;8(23):1800120.
108. Lei Y, Wang Z, Bao A, et al. Recent advances on electrocatalytic CO_2 reduction to resources: target products, reaction pathways and typical catalysts. *Chem Eng J*. 2023;453.
109. Shi YCN, Cao T, Zhang J. Solid oxide electrolysis cells. In: *High-temperature Electrochemical Energy Conversion and Storage: Fundamentals and Applications*. CRC Press; 2017:p 68.
110. Gu X-K, Carneiro JSA, Nikolla E. First-principles study of high temperature CO_2 electrolysis on transition metal electrocatalysts. *Ind Eng Chem Res*. 2017;56(21):6155–6163.
111. Kozokaro VF, Addo PK, Ansari HM, Birss VI, Toroker MC. Optimal oxygen vacancy concentration for CO_2 reduction in LSFCr perovskite: a combined density functional theory and thermogravimetric analysis measurement study. *J Phys Chem C*. 2020;124(50):27453–27466.
112. Yang Y, Li Y, Jiang Y, et al. The electrochemical performance and CO_2 reduction mechanism on strontium doped lanthanum ferrite fuel electrode in solid oxide electrolysis cell. *Electrochim Acta*. 2018;284:159–167.
113. Tezel E, Guo D, Whitten A, et al. Elucidating the role of B-site cations toward CO_2 reduction in perovskite-based solid oxide electrolysis cells. *J Electrochem Soc*. 2022;169(3), 034532.
114. Ren B, Croiset E, Ricardez–Sandoval L. A theoretical study on CO_2 electrolysis through synergistic manipulation of Ni/Mn doping and oxygen vacancies in La(Sr)FeO_3. *J Catal*. 2020;383:273–282.
115. Irvine JTS. e. a., Perovskite oxide anodes for SOFCs. In: Ishihara T, ed. *Perovskite Oxide for Solid Oxide Fuel Cells*. 2009. Springer.
116. Song Y, Zhang X, Xie K, Wang G, Bao X. High-temperature CO_2 electrolysis in solid oxide electrolysis cells: developments, challenges, and prospects. *Adv Mater*. 2019;31(50):1902033.
117. Lv H, Lin L, Zhang X, et al. In situ exsolved $FeNi_3$ nanoparticles on nickel doped $Sr_2Fe_{1.5}Mo_{0.5}O_{6-\delta}$ perovskite for efficient electrochemical CO_2 reduction reaction. *J Mater Chem*. 2019;7(19):11967–11975.
118. Irvine JTS, Connor PA, et al. Solid oxide fuels cells: facts and figures. *Springer: London*. 2013.
119. Adler SB. Factors governing oxygen reduction in solid oxide fuel cell cathodes. *Chem. Rev*. 2004;104(10):4791–4844.

120. Mori M, Hiei Y, Sammes NM, Tompsett GA. Thermal-expansion behaviors and mechanisms for Ca-or Sr-doped lanthanum manganite perovskites under oxidizing atmospheres. *J Solid State Electrochem*. 2000;147(4):1295–1302.
121. Jiang SP. Development of lanthanum strontium manganite perovskite cathode materials of solid oxide fuel cells: a review. *J Mater Sci*. 2008;43(21):6799–6833.
122. Zhang Y, Zhao H, Du Z, Świerczek K, Li Y. High-performance $SmBaMn_2O_{5+\delta}$ electrode for symmetrical solid oxide fuel cell. *Chem Mater*. 2019;31(10):3784–3793.
123. Adler SB, Lane JA, Steele BCH. Electrode kinetics of porous mixed-conducting oxygen electrodes. *J Electrochem Soc*. 1996;143(11):3554–3564.
124. Sun C, Hui R, Roller J. Cathode materials for solid oxide fuel cells: a review. *J Solid State Electrochem*. 2009;14(7):1125–1144.
125. Shao Z, Haile SM. A high-performance cathode for the next generation of solid-oxide fuel cells. *Nature*. 2004;431(7005):170–173.
126. Kim JH, Kim Y, Connor PA, Irvine JTS, Bae J, Zhou W. Structural, thermal and electrochemical properties of layered perovskite $SmBaCo_2O_{5+d}$, a potential cathode material for intermediate-temperature solid oxide fuel cells. *J Power Sources*. 2009;194(2):704–711.
127. Amow G, Davidson I, Skinner S. A comparative study of the Ruddlesden-Popper series, $La_{n+1}Ni_nO_{3n+1}$ (n=1, 2 and 3), for solid-oxide fuel-cell cathode applications. *Solid State Ionics*. 2006;177(13-14):1205–1210.
128. Islam MS, Davies RA. Atomistic study of dopant site-selectivity and defect association in the lanthanum gallate perovskite. *J Mater Chem*. 2004;14(1):86–93.
129. Badwal SPS. Zirconia-based solid electrolytes: microstructure, stability and ionic conductivity. *Solid State Ionics*. 1992;52(1-3):23–32.
130. Wachsman ED, Lee KT. D, Lowering the temperature of solid oxide fuel cells. *Science. 2011*. 2011;334(6058):935–939.
131. Ishihara T, Matsuda H, Takita Y. Doped $LaGaO_3$ perovskite type oxide as a new oxide ionic conductor. *J Am Chem Soc*. 1994;116(9):3801–3803.
132. Malavasi L, Fisher CA, Islam MS. Oxide-ion and proton conducting electrolyte materials for clean energy applications: structural and mechanistic features. *Chem Soc Rev*. 2010;39(11):4370–4387.
133. Ge X-M, Chan S-H, Liu Q-L, Sun Q. Solid oxide fuel cell anode materials for direct hydrocarbon utilization. *Adv Energy Mater*. 2012;2(10):1156–1181.
134. Müller AC, Herbstritt D, Ivers-Tiffée E. Development of a multilayer anode for solid oxide fuel cells. *Solid State Ionics*. 2002;152:537–542.
135. Gross MD, Vohs JM, Gorte RJ. Recent progress in SOFC anodes for direct utilization of hydrocarbons. *J Mater Chem*. 2007;17(30):3071–3077.
136. Cheng Z, Liu M. Characterization of sulfur poisoning of Ni–YSZ anodes for solid oxide fuel cells using in situ Raman microspectroscopy. *Solid State Ionics*. 2007;178(13-14):925–935.
137. Zheng LL, Wang X, Zhang L, Wang J-Y, Jiang SP. Effect of Pd-impregnation on performance, sulfur poisoning and tolerance of Ni/GDC anode of solid oxide fuel cells. *Int J Hydrogen Energy*. 2012;37(13):10299–10310.
138. Kan H, Lee H. Enhanced stability of Ni–Fe/GDC solid oxide fuel cell anodes for dry methane fuel. *Catal Commun*. 2010;12(1):36–39.
139. Grgicak CM, Pakulska MM, O'Brien JS, Giorgi JB. Synergistic effects of $Ni_{1-x}Co_x$-YSZ and $Ni_{1-x}Cu_x$-YSZ alloyed cermet SOFC anodes for oxidation of hydrogen and methane fuels containing H_2S. *J Power Sources*. 2008;183(1):26–33.
140. Park S, Vohs JM, Gorte RJ. Direct oxidation of hydrocarbons in a solid-oxide fuel cell. *Nature*. 2000;404(775):265–267.
141. Cai G, Liu R, Zhao C, Li J, Wang S, Wen T. Anode performance of Mn-doped ceria–ScSZ for solid oxide fuel cell. *J Solid State Electrochem*. 2010;15(1):147–152.
142. Yan N, Pandey J, Zeng Y, et al. Developing a thermal- and coking-resistant cobalt–tungsten bimetallic anode catalyst for solid oxide fuel cells. *ACS Catal*. 2016;6(7):4630–4634.
143. Wuensch BJ, Eberman KW, Heremans C, et al. Connection between oxygen-ion conductivity of pyrochlore fuel-cell materials and structural change with composition and temperature. *Solid State Ionics*. 2000;129(1-4):111–133.
144. Cowin PI, Petit CTG, Lan R, Irvine JTS, Tao S. Recent progress in the development of anode materials for solid oxide fuel cells. *Adv Energy Mater*. 2011;1(3):314–332.
145. Bidrawn F, Kim G, Corre G, Irvine JTS, Vohs JM, Gorte RJ. Efficient reduction of CO_2 in a solid oxide electrolyzer. *Electrochem Solid State Lett*. 2008;11(9):B167–B170.
146. Hu S, Zhang L, Cai L, et al. Iron stabilized 1/3 A-site deficient La–Ti–O perovskite cathodes for efficient CO_2 electroreduction. *J Mater Chem*. 2020;8(40):21053–21061.
147. Wang M, Li N, Shen Q, Zhan Z, Chen C. A highly efficient and stable perovskite cathode with in situ exsolved NiFe alloy nanoparticles for CO_2 electrolysis. *Sustain Energy Fuels*. 2022;6(8):2038–2044.
148. Li H, Sun G, Xie K, et al. Chromate cathode decorated with in-situ growth of copper nanocatalyst for high temperature carbon dioxide electrolysis. *Int J Hydrogen Energy*. 2014;39(36):20888–20897.
149. Qi W, Xie K, Liu M, et al. Single-phase nickel-doped ceria cathode with in situ grown nickel nanocatalyst for direct high-temperature carbon dioxide electrolysis. *RSC Adv*. 2014;4(76):40494–40504.
150. Wei H, Xie K, Zhang J, et al. In situ growth of Ni_xCu_{1-x} alloy nanocatalysts on redox-reversible rutile $(Nb,Ti)O_4$ towards high-temperature carbon dioxide electrolysis. *Sci Rep*. 2014;4:5156.
151. Xie K, Zhang J, Xu S, et al. Composite cathode based on redox-reversible $NbTi_{0.5}Ni_{0.5}O_4$ decorated with in-situ grown Ni particles for direct carbon dioxide electrolysis. *Fuel Cell*. 2014;14(6):1036–1045.
152. Li Y, Xie K, Chen S, Li H, Zhang Y, Wu Y. Efficient carbon dioxide electrolysis based on perovskite cathode enhanced with nickel nanocatalyst. *Electrochim Acta*. 2015;153:325–333.
153. Yang L, Xue X, Xie K. Spatially confined catalysis-enhanced high-temperature carbon dioxide electrolysis. *Phys Chem Chem Phys*. 2015;17(17):11705–11714.
154. Ruan C, Xie K. A redox-stable chromate cathode decorated with in situ grown nickel nanocatalyst for efficient carbon dioxide electrolysis. *Catal Sci Technol*. 2015;5(3):1929–1940.
155. Wang S, Tsuruta H, Asanuma M, Ishihara T. Ni-Fe-La(Sr)Fe(Mn)O_3 as a new active cermet cathode for intermediate-temperature CO_2 electrolysis using a $LaGaO_3$-based electrolyte. *Adv Energy Mater*. 2015;5(2).
156. Gan L, Ye L, Tao S, Xie K. Titanate cathodes with enhanced electrical properties achieved via growing surface Ni particles toward efficient carbon dioxide electrolysis. *Phys Chem Chem Phys*. 2016;18(4):3137–3143.
157. Liu S, Liu Q, Luo J-L. CO_2-to-CO conversion on layered perovskite with in situ exsolved Co–Fe alloy nanoparticles: an active and stable cathode for solid oxide electrolysis cells. *J Mater Chem*. 2016;4(44):17521–17528.
158. Ye L, Pan C, Zhang M, et al. Highly efficient CO_2 electrolysis on cathodes with exsolved alkaline earth oxide nanostructures. *ACS Appl Mater Interfaces*. 2017;9(30):25350–25357.
159. Zhu C, Hou S, Hou L, Xie K. Perovskite $SrFeO_{3-\delta}$ decorated with Ni nanoparticles for high temperature carbon dioxide electrolysis. *Int J Hydrogen Energy*. 2018;43(36):17040–17047.
160. Tian Y, Zhang L, Jia L, et al. Novel quasi-symmetrical solid oxide electrolysis cells with in-situ exsolved cathode for CO_2 electrolysis. *J CO2 Util*. 2019;31:43–50.
161. Hu X, Xie K. Active and stable Ni/$Cr_2O_{3-\delta}$ cathodes for high temperature CO_2 electrolysis. *J Power Sources*. 2019;430:20–24.
162. Wang W, Gan L, Lemmon JP, Chen F, Irvine JTS, Xie K. Enhanced carbon dioxide electrolysis at redox manipulated interfaces. *Nat Commun*. 2019;10(1):1550.
163. Kyriakou V, Neagu D, Zafeiropoulos G, et al. Symmetrical exsolution of Rh nanoparticles in solid oxide cells for efficient syngas production from greenhouse gases. *ACS Catal*. 2019;10(2):1278–1288.
164. Hu S, Zhang L, Liu H, et al. Detrimental phase evolution triggered by Ni in perovskite-type cathodes for CO_2 electroreduction. *J Energy Chem*. 2019;36:87–94.
165. Kyriakou V, Neagu D, Papaioannou EI, Metcalfe IS, van de Sanden MCM, Tsampas MN. Co-electrolysis of H_2O and CO_2 on exsolved Ni nanoparticles for efficient syngas generation at controllable H_2/CO ratios. *Appl Catal B Environ*. 2019;258:117950.
166. Yang Y, Wang Y, Yang Z, Chen Y, Peng S. A highly active and durable electrode with in situ exsolved Co nanoparticles for solid oxide electrolysis cells. *J Power Sources*. 2020;478:229082.
167. Zhu J, Zhang W, Li Y, Yue W, Geng G, Yu B. Enhancing CO_2 catalytic activation and direct electroreduction on in-situ exsolved Fe/MnO_x nanoparticles from $(Pr,Ba)_2Mn_{2-y}Fe_yO_{5+\delta}$ layered perovskites for SOEC cathodes. *Appl Catal B Environ*. 2020;268:118389.
168. Xi X, Wang X-W, Fan Y, et al. Efficient bifunctional electrocatalysts for solid oxide cells based on the structural evolution of perovskites with abundant defects and exsolved CoFe nanoparticles. *J Power Sources*. 2021;482:228981.
169. Ding S, Li M, Pang W, et al. A-site deficient perovskite with nano-socketed Ni-Fe alloy particles as highly active and durable catalyst for high-temperature CO_2 electrolysis. *Electrochim Acta*. 2020;335:135683.
170. Bai L, Li H, Yan Z, et al. New insight into the doped strontium titanate cathode with in situ exsolved nickel nanoparticles for electrolysis of carbon dioxide. *Adv Mater Interfac*. 2021;8(3):2001598.
171. Lv H, Liu T, Zhang X, et al. Atomic-scale insight into exsolution of CoFe alloy nanoparticles in $La_{0.4}Sr_{0.6}Co_{0.2}Fe_{0.7}Mo_{0.1}O_{3-\delta}$ with efficient CO_2 electrolysis. *Angew Chem Int Ed*. 2020;59(37):15968–15973.
172. Lv H, Lin L, Zhang X, et al. Situ investigation of reversible exsolution/dissolution of CoFe alloy nanoparticles in a Co-doped $Sr_2Fe_{1.5}Mo_{0.5}O_{6-\delta}$ cathode for CO_2 electrolysis. *Adv Mater*. 2020;32(6), e1906193.
173. Park S, Kim Y, Noh Y, et al. A sulfur-tolerant cathode catalyst fabricated with in situ exsolved CoNi alloy nanoparticles anchored on a Ruddlesden–Popper support for CO_2 electrolysis. *J Mater Chem*. 2020;8(1):138–148.
174. Hu S, Li H, Dong X, et al. Rational design of CO_2 electroreduction cathode via in situ electrochemical phase transition. *J Energy Chem*. 2022;66:603–611.
175. Liu C, Li S, Gao J, et al. Enhancing CO_2 catalytic adsorption on an Fe nanoparticle-decorated $LaSrFeO_{4+\delta}$ cathode for CO_2 electrolysis. *ACS Appl Mater Interfaces*. 2021;13(7):8229–8238.
176. Choi J, Park S, Han H, et al. Highly efficient CO_2 electrolysis to CO on Ruddlesden–Popper perovskite oxide with in situ exsolved Fe nanoparticles. *J Mater Chem*. 2021;9(13):8740–8748.
177. Lv H, Lin L, Zhang X, et al. Promoting exsolution of RuFe alloy nanoparticles on $Sr_2Fe_{1.4}Ru_{0.1}Mo_{0.5}O_{6-\delta}$ via repeated redox manipulations for CO_2 electrolysis. *Nat Commun*. 2021;12(1):5665.
178. Xi X, Fan Y, Zhang J, Luo J-L, Fu X-Z. In-situ construction of hetero-structured perovskite composites with exsolved Fe and Cu metallic nanoparticles as efficient CO_2 reduction electrocatalyst for high performance solid oxide electrolysis cells. *J Mater Chem*. 2021;10(5):2509–2518.
179. Yang X, Sun W, Ma M, et al. Achieving highly efficient carbon dioxide electrolysis by in Situ construction of the heterostructure. *ACS Appl Mater Interfaces*. 2021;13(17):20060–20069.

180. He D, Ruan W, Li J, Ni J, Ni C. Heterogeneity in the Mo doped $La_{0.55}Sr_{0.45}FeO_3$ cathode for direct CO_2 electrolysis. *Chem Eng J*. 2022;433:133632.
181. Lv J, Sun W, Xu C, et al. Enhancing the catalytic activity and CO_2 chemisorption ability of the perovskite cathode for soild oxide electrolysis cell through in situ Fe-Sn alloy nanoparticles. *Sep Purif Technol*. 2022;294:121127.
182. Zhang D, Yang W, Wang Z, et al. Efficient electrochemical CO_2 reduction reaction on a robust perovskite type cathode with in-situ exsolved Fe-Ru alloy nanocatalysts. *Sep Purif Technol*. 2023;304:122287.
183. Li P, Xuan Y, Jiang B, Zhang S, Xia C. Hollow $La_{0.6}Sr_{0.4}Ni_{0.2}Fe_{0.75}Mo_{0.05}O_{3-\delta}$ electrodes with exsolved $FeNi_3$ in quasi-symmetrical solid oxide electrolysis cells for direct CO_2 electrolysis. *Electrochem Commun*. 2022;134:107188.
184. Li J, Liu Q, Song Y, et al. In-situ exsolution of cobalt nanoparticles from $La_{0.5}Sr_{0.5}Fe_{0.8}Co_{0.2}O_{3-\delta}$ cathode for enhanced CO_2 electrolysis performance. *Green Chemical Engineering*. 2022;3(3):250–258.
185. Zhang S, Jiang Y, Han H, Li Y, Xia C. Perovskite oxyfluoride ceramic with in Situ exsolved Ni-Fe nanoparticles for direct CO_2 electrolysis in solid oxide electrolysis cells. *ACS Appl Mater Interfaces*. 2022;14(25):28854–28864.
186. Tan T, Wang Z, Qin M, et al. In situ exsolution of core-shell structured $NiFe/FeO_x$ nanoparticles on $Pr_{0.4}Sr_{1.6}(NiFe)_{1.5}Mo_{0.5}O_{6-\delta}$ for CO_2 electrolysis. *Adv Funct Mater*. 2022;32(34):2202878.
187. Sun X, Ye Y, Zhou M, et al. Layered-perovskite oxides with in situ exsolved Co–Fe alloy nanoparticles as highly efficient electrodes for high-temperature carbon dioxide electrolysis. *J Mater Chem*. 2022;10(5):2327–2335.
188. Li Z, Peng M, Zhu Y, et al. The facilitated cathodic elementary reactions of solid oxide electrolysis cells for CO_2 conversion over a Ce decorated $La_{0.43}Ca_{0.37}Ti_{0.94}N_{i0.06}O_{3-\delta}$ electrocatalyst. *J Mater Chem*. 2022;10(38):20350–20364.
189. Zheng Y, Qian B, Wang S, et al. Ca-Fe co-doped $La_{0.75}Sr_{0.25}Cr_{0.5}Mn_{0.5}O_3$ cathodes with high electrocatalytic activity for direct CO_2 electrolysis in solid oxide electrolysis cells. *J CO2 Util*. 2022;67:102305.
190. Zhang Y, Xu Y, Gan L. Exsolved metallic iron nanoparticles in perovskite cathode to enhance CO_2 electrolysis. *J Solid State Electrochem*. 2022;26(2):409–417.
191. Tian Y, Yang C, Wang Y, et al. Phase transition with in situ exsolution nanoparticles in the reduced $Pr_{0.5}Ba_{0.5}Fe_{0.8}Ni_{0.2}O_{3-\delta}$ electrode for symmetric solid oxide cells. *J Mater Chem*. 2022;10(31):16490–16496.
192. Jiang Y, Ye L, Zhang S, Xia C. Doped ceria with exsolved Fe^0 nanoparticles as a Sr-free cathode for CO_2 electrolysis in SOECs at reduced temperatures. *J Mater Chem*. 2022;10(17):9380–9383.
193. Liu S, Xu Y, Xie K, Ye L, Gan L. Enhancing CO_2 electrolysis through engineering atomic oxygen transfer at interfaces. *Sep Purif Technol*. 2022;288:120704.
194. Pang B, Hu S, Zhang L, Zhang P, Zhu X, Yang W. Non-perovskite structural $CaFe_2O_4$ with matched thermal expansion coefficients exhibiting high performance for CO_2 electroreduction. *ACS Sustainable Chem Eng*. 2022;10(36):11969–11976.
195. He F, Hou M, Zhu F, et al. Building efficient and durable hetero-interfaces on a perovskite-based electrode for electrochemical CO_2 reduction. *Adv Energy Mater*. 2022;12(43):2202175.
196. Xu M, Liu C, Naden AB, Früchtl H, Bühl M, Irvine JTS. Electrochemical activation applied to perovskite titanate fibers to yield supported alloy nanoparticles for electrocatalytic application. *Small*. 2022;19(1):2204682.
197. Carneiro J, Gu X-K, Tezel E, Nikolla E. Electrochemical reduction of CO_2 on metal-based cathode electrocatalysts of solid oxide electrolysis cells. *Ind Eng Chem Res*. 2020;59(36):15884–15893.
198. Cong Y, Geng Z, Zhu Q, et al. Cation-exchange-induced metal and alloy dual-exsolution in perovskite ferrite oxides boosting the performance of Li-O_2 battery. *Angew Chem Int Ed*. 2021;60(43):23380–23387.
199. Hu Y, Wu J, Han Y, et al. Intensified solar thermochemical CO_2 splitting over iron-based redox materials via perovskite-mediated dealloying-exsolution cycles. *Chin J Catal*. 2021;42(11):2049–2058.
200. De Trizio L, Manna L. Forging colloidal nanostructures via cation exchange reactions. *Chem. Rev*. 2016;116(18):10852–10887.
201. Jo S, Han Kim Y, Jeong H, et al. Exsolution of phase-separated nanoparticles via trigger effect toward reversible solid oxide cell. *Appl Energy*. 2022;323:119615.
202. Jiang Y, Geng Z, Sun Y, et al. Highly efficient B-site exsolution assisted by co doping in lanthanum ferrite toward high-performance electrocatalysts for oxygen evolution and oxygen reduction. *ACS Sustainable Chem Eng*. 2019;8(1):302–310.
203. Sun C, Bian L, Qi J, et al. Boosting CO_2 directly electrolysis by electron doping in $Sr_2Fe_{1.5}Mo_{0.5}O_{6-\delta}$ double perovskite cathode. *J Power Sources*. 2022;521:230984.
204. Duan N, Yang J, Gao M, et al. Multi-functionalities enabled fivefold applications of $LaCo_{0.6}Ni_{0.4}O_{3-\delta}$ in intermediate temperature symmetrical solid oxide fuel/electrolysis cells. *Nano Energy*. 2020;77:105207.
205. Sengodan S, Choi S, Jun A, et al. Layered oxygen-deficient double perovskite as an efficient and stable anode for direct hydrocarbon solid oxide fuel cells. *Nat Mater*. 2015;14(2):205–209.
206. Kim H, Lim C, Kwon O, et al. Unveiling the key factor for the phase reconstruction and exsolved metallic particle distribution in perovskites. *Nat Commun*. 2021;12(1):6814.
207. Wu X, Yu Y, Chen Y, Li L, Ma ZF, Yin YM. Construction of multifunctional nanoarchitectures in one step on a composite fuel catalyst through in situ exsolution of $La_{0.5}Sr_{0.5}Fe_{0.8}Ni_{0.1}Nb_{0.1}O_{3-\delta}$. *ACS Appl Mater Interfaces*. 2020;12(31):34890–34900.
208. Zhang X, Ye L, Xie K. Electrochemical reduction of CO_2 with exsolved metal–oxide interfaces in a proton-conducting solid oxide electrolyzer. *Energy Fuel*. 2022;36(19):11576–11583.
209. Lindenthal L, Popovic J, Rameshan R, et al. Novel perovskite catalysts for CO_2 utilization-Exsolution enhanced reverse water-gas shift activity. *Appl Catal B Environ*. 2021;292:120183.
210. He S, Li M, Hui J, Yue X. In-situ construction of ceria-metal/titanate heterostructure with controllable architectures for efficient fuel electrochemical conversion. *Appl Catal B Environ*. 2021;298:120588–120598.
211. Li Y, Li Y, Yu L, et al. Achieving excellent and durable CO_2 electrolysis performance on a dual-phase fuel electrode in solid oxide electrolysis cells. *J Power Sources*. 2021;491:229599.
212. Deka DJ, Kim J, Gunduz S, et al. Coke formation during high-temperature CO_2 electrolysis over $AFeO_3$ (A = La/Sr) cathode: effect of A-site metal segregation. *Appl Catal B Environ*. 2021;283:119642.
213. Lindenthal L, Huber J, Drexler H, et al. In situ growth of exsolved nanoparticles under varying rWGS reaction conditions—a catalysis and near ambient pressure-XPS study. *Catalysts*. 2021;11(12):1484.
214. Myung JH, Neagu D, Miller DN, Irvine JTS. Switching on electrocatalytic activity in solid oxide cells. *Nature*. 2016;537(7621):528–531.
215. Chanthanumataporn M, Hui J, Yue X, Kakinuma K, Irvine JTS, Hanamura K. Electrical reduction of perovskite electrodes for accelerating exsolution of nanoparticles. *Electrochim Acta*. 2019;306:159–166.
216. Yue X, Pukhova A, He S, Zhang N. Examining operando generated Ni-based alloy nanomaterials as fuel electrodes in solid oxide cells. *J Electrochem Soc*. 2021;168(10):104514.
217. Opitz AK, Nenning A, Rameshan C, et al. Surface chemistry of perovskite-type electrodes during high temperature CO_2 electrolysis investigated by operando photoelectron spectroscopy. *ACS Appl Mater Interfaces*. 2017;9(41):35847–35860.
218. Hu S, Zhang L, Cao Z, et al. Cathode activation process and CO_2 electroreduction mechanism on $LnFeO_{3-\delta}$ (Ln=La, Pr and Gd) perovskite cathodes. *J Power Sources*. 2021;485.
219. Zhang K, Zhao Y, He W, et al. Pr and Mo co-doped $SrFeO_{3-\delta}$ as an efficient cathode for pure CO_2 reduction reaction in a solid oxide electrolysis cell. *Energy Technol*. 2020;8(10).
220. Zhou W, Shao Z, Liang F, et al. A new cathode for solid oxide fuel cells capable of in situ electrochemical regeneration. *J Mater Chem*. 2011;21(39):15343–15351.
221. Fan W, Wang B, Gao R, et al. Anodic shock-triggered exsolution of metal nanoparticles from perovskite oxide. *J Am Chem Soc*. 2022;144(17):7657–7666.
222. Yao W, Duan T, Li Y, Yang L, Xie K. Perovskite chromate doped with titanium for direct carbon dioxide electrolysis. *New J Chem*. 2015;39(4):2956–2965.
223. Li J, Ye L, Xie K. Enhanced CO_2 electrolysis at metal–oxide interfaces. *J Solid State Electrochem*. 2022;26(3):773–782.
224. Chueh WC, Hao Y, Jung W, Haile SM. High electrochemical activity of the oxide phase in model ceria-Pt and ceria-Ni composite anodes. *Nat Mater*. 2011;11(2):155–161.
225. Chen D, Guan Z, Zhang D, et al. Constructing a pathway for mixed ion and electron transfer reactions for O_2 incorporation in $Pr_{0.1}Ce_{0.9}O_{2-x}$. *Nat. Catal*. 2020;3(2):116–124.
226. Sullivan TA, Linne D, Bryant L, Kennedy K. In-situ-produced methane and methane/carbon monoxide mixtures for return propulsion from Mars. *J Propul Power*. 1995;11(5):1056–1062.
227. K.R. Sridhar B. T. V., Oxygen production on Mars using solid oxide electrolysis. *Solid State Ionics*. 1997;93:321–328.
228. Zheng Y, Jiang H, Wang S, et al. Mn-doped Ruddlesden-Popper oxide $La_{1.5}Sr_{0.5}NiO_{4+\delta}$ as a novel air electrode material for solid oxide electrolysis cells. *Ceram Int*. 2021;47(1):1208–1217.
229. Gan J, Hou N, Yao T, et al. A high performing perovskite cathode with in situ exsolved Co nanoparticles for H_2O and CO_2 solid oxide electrolysis cell. *Catal Today*. 2021;364:89–96.
230. Skafte TL, Guan Z, Machala ML, et al. Selective high-temperature CO_2 electrolysis enabled by oxidized carbon intermediates. *Nat Energy*. 2019;4(10):846–855.
231. Zhang C, Grass ME, Yu Y, et al. Multielement activity mapping and potential mapping in solid oxide electrochemical cells through the use of operando XPS. *ACS Catal*. 2012;2(11):2297–2304.
232. Choi Y, Cha SK, Ha H, et al. Unravelling inherent electrocatalysis of mixed-conducting oxide activated by metal nanoparticle for fuel cell electrodes. *Nat Nanotechnol*. 2019;14(3):245–251.
233. Wang J, Syed K, Ning S, et al. Exsolution synthesis of nanocomposite perovskites with tunable electrical and magnetic properties. *Adv Funct Mater*. 2021;32(9):2108005.
234. Hu Sulei. W.-X. L., Sabatier principle of metal-support interaction for design of ultrastable metal nanocatalysts. *Science*. 2022;374:1360–1365.
235. Zhai S, Xie H, Cui P, et al. A combined ionic Lewis acid descriptor and machine-learning approach to prediction of efficient oxygen reduction electrodes for ceramic fuel cells. *Nat Energy*. 2022;7(9):866–875.
236. Xu H, Ma J, Tan P, et al. Towards online optimisation of solid oxide fuel cell performance: combining deep learning with multi-physics simulation. *Energy and AI*. 2020;1:100003.
237. Zhong M, Tran K, Min Y, et al. Accelerated discovery of CO_2 electrocatalysts using active machine learning. *Nature*. 2020;581(7807):178–183.

Min Xu received his Ph.D. in Chemistry, University of St Andrews in 2022, and his bachelor and master degree in University of Electronic and Technology of China, in 2014 and 2017. He is now a postdoctoral fellow in Tsinghua University. His main research interests are oxide materials, electrochemistry and solid oxide fuel/electrolysis cells, especially the evolution responds of oxide electrode materials under device operating conditions, such as high temperature, potential and various fuels.

Di Chen received his bachelor's degree from the Department of Materials Science and Engineering at Tsinghua University, and his doctorate degree from the Department of Materials Science and Engineering at MIT. He received his postdoc training at Stanford University. He joined the Future Laboratory at Tsinghua University in 2019. His current research interests include electroceramics, high-temperature electrochemistry, and energy conversion systems such solid oxide fuel cells and electrolysis cells.